A trans-eQTL network regulates osteoclast multinucleation and bone mass

Marie Pereira[1,2], Jeong-Hun Ko[1,2], John Logan[2], Hayley Protheroe[2], Kee-Beom Kim[3], Amelia Li Min Tan[5], Kwon-Sik Park[3], Maxime Rotival[4], Enrico Petretto[5], J. H. Duncan Bassett[2], Graham R. Williams[2], Jacques Behmoaras[1]

[1]Centre for Inflammatory Disease, Department of Immunology and Inflammation, Hammersmith Hospital, Imperial College London, Du Cane Road W12 0NN, London, UK

[2]Molecular Endocrinology Laboratory, Department of Metabolism, Digestion & Reproduction, Hammersmith Hospital, Imperial College London, Du Cane Road W12 0NN, London, UK

[3]Department of Microbiology, Immunology, and Cancer Biology, University of Virginia School of Medicine, Charlottesville, VA 22908, USA.

[4]Human Evolutionary Genetics Unit, Institut Pasteur, Centre National de la Recherche Scientifique, UMR 2000, 75015 Paris, France.

[5]Duke-NUS Medical School, Singapore, Singapore.

Correspondence to be addressed to Jacques Behmoaras (jacques.behmoaras@imperial.ac.uk) or Duncan Bassett (d.bassett@imperial.ac.uk) or Graham Williams (graham.williams@imperial.ac.uk)

Abstract

Functional characterisation of cell-type specific regulatory networks is key to establish a causal link between genetic variation and phenotype. The osteoclast offers a unique model for interrogating the contribution of co-regulated genes to *in vivo* phenotype as its multinucleation and resorption activities determine quantifiable skeletal traits. Here we took advantage of a *trans*-regulated gene network (MMnet, macrophage multinucleation network) which we found to be significantly enriched for GWAS variants associated with bone-related phenotypes. We found that the network hub gene *Bcat1* and seven other co-regulated MMnet genes out of 13, regulate bone function. Specifically, global (*Pik3cb*$^{-/-}$, *Atp8b2*$^{+/-}$, *Igsf8*$^{-/-}$, *Eml1*$^{-/-}$, *Appl2*$^{-/-}$, *Deptor*$^{-/-}$) and myeloid-specific *Slc40a1*$^{\Delta LysMCre}$ knockout mice displayed abnormal bone phenotypes. We report antagonizing effects of MMnet genes on bone mass in mice and osteoclast multinucleation/resorption in humans with strong correlation between the two. These results identify MMnet as a functionally conserved network that regulates osteoclast fusion and bone mass.

Impact statement: We took advantage of the osteoclast whose multinucleation properties correlate with bone mass. We show that a *trans*-regulated gene network (MMnet) controls skeletal homeostasis through osteoclast multinucleation and function.

Introduction

The large number of common genetic variants associated with prevalent complex diseases suggests that disease pathogenesis involves perturbations to intricate gene networks (Furlong, 2013). The recently proposed omnigenic model of complex traits highlights the importance of *trans*-regulated networks in understanding causative disease pathways (Boyle et al., 2017; Liu et al., 2019). One way of mapping these regulatory networks is to identify the genetic control points of gene co-expression networks in a cell type relevant to the disease of interest. In this way, expression quantitative trait loci (eQTL) studies have revealed regions of the genome that harbour sequence variants affecting the mRNA expression levels of one or more genes (Albert and Kruglyak, 2015). These approaches identified *trans*-eQTLs, which regulate gene expression that are often observed in clusters, also known as *trans*-eQTL hotspots (Albert et al., 2018; Brem et al., 2002; Morley et al., 2004; Schadt et al., 2003). Many of the *trans*-eQTLs discovered to date in different model organisms tend to influence the expression of multiple genes (Albert et al., 2018; Bagnati et al., 2019; Battle et al., 2014; Brynedal et al., 2017; Fehrmann et al., 2011; Grundberg et al., 2012; Heinig et al., 2010; Johnson et al., 2015; Kang et al., 2014; Lee et al., 2014; Small et al., 2011; Wright et al., 2014; Yao et al., 2017), which suggests coordinated (network-based) regulatory mechanisms might be perturbed during disease pathogenesis. Although identification of such networks has informed our understanding of gene-gene interactions, their functional validation remains challenging.

Bone-resorbing multinucleated osteoclasts are derived from the monocyte-macrophage lineage (Pereira et al., 2018). They display high metabolic activity (Indo et al., 2013) and regulate bone mass, structure and strength. Abnormal osteoclastic bone resorption is a major underlying cause of both low and high bone mass disorders including osteoporosis (Manolagas, 2010), and osteopetrosis (Sobacchi et al., 2013), and an important contributor to the pathogenesis of Paget's disease (Galson and Roodman, 2014), adolescent idiopathic scoliosis (AIS) (Liu et al., 2018), and inflammatory diseases that affect the skeleton such as

rheumatoid arthritis, ankylosing spondylitis and periodontitis (DiCarlo and Kahn, 2011; McInnes and Schett, 2011). Recent genome-wide association studies (GWAS) have identified hundreds of polymorphic loci associated with bone diseases in humans, including many that contain osteoclast-related genes (Albagha et al., 2010; Estrada et al., 2012; Kemp et al., 2017; Kim, 2018; Medina-Gomez et al., 2018; Morris et al., 2019; Stahl et al., 2010). However, only a few causal genes have been implicated in disease onset and progression, suggesting that activities of complex interacting gene networks play a crucial role in establishing and optimising bone mass and strength and in the pathogenesis of skeletal disease (Al-Barghouthi and Farber, 2019).

We previously developed a rapid-throughput skeletal phenotyping pipeline that combines both structural and functional parameters (Bassett et al., 2012a; Freudenthal et al., 2016). We first applied this multi-parameter phenotyping pipeline to analyse 100 knockout (KO) mice and reported 9 new genetic determinants of bone mineralisation, structure and strength (Bassett et al., 2012a). We then extended our studies to over 500 KO mouse lines and integrated this large-scale phenotype resource with over 1000 conditionally independent SNPs at over 500 loci that significantly associate with bone mineral density (BMD) and fracture in GWAS to provide functional evidence of causation for candidate genes (Kemp et al., 2017; Medina-Gomez et al., 2018; Morris et al., 2019; Trajanoska et al., 2018). These integrative studies demonstrated how large-scale phenotyping and genetic association studies provide systems-level platforms for gene identification in skeletal disorders. Robust systems genetics approaches also incorporate functional assays in a context-dependent cell type such that the effect of genome variation can be investigated to identify cell-specific mechanisms of disease. The osteoclast has an important advantage as its multinucleation capability correlates with its resorptive activity as well as with quantitative *in vivo* traits such as bone mass, structure and strength (Pereira et al., 2018). Thus, we hypothesise that osteoclast gene regulatory networks play a key role to establish and maintain optimal bone structure and strength, and are perturbed in skeletal disease.

We previously investigated the genetic determinants of macrophage multinucleation, using the inbred Wistar Kyoto (WKY) rat strain that displays spontaneous macrophage fusion (Kang et al., 2014). By mapping eQTLs in fusion-competent primary macrophages, we found a *trans*-regulated gene co-expression network (190 genes) enriched for osteoclast genes that we defined as a "macrophage multinucleation network" (MMnet) (Kang et al., 2014). MMnet is under the genetic control of the *Trem2* locus and includes a hub gene, *Bcat1* that has the greatest number of connections (i.e. co-expression) with other MMnet transcripts. This network contained *trans*-regulated genes previously involved in osteoclastogenesis and we defined a new role for the most significant *trans*-eQTL (*Kcnn4*) in osteoclast multinucleation, bone homeostasis and inflammatory arthritis (Kang et al., 2014).

Here we validate the functional role of MMnet in the regulation of osteoclast multinucleation, resorption and bone mass and strength. We report a robust correlation between the profound effects of MMnet gene knockdown on multinucleation and resorption *in vitro* and the effect on bone mass *in vivo*. Our study illustrates how the cell specific function of osteoclast multinucleation and resorption can be used to link genetic variation within a complex network of co-regulated genes to the clinically critical phenotypes of bone mass and strength.

Materials and methods

Animals

14 week-old male Wistar-Kyoto (WKY/NCrl) and Lewis (LEW/Crl) rats were purchased from Charles River. *Bcat1* knockout (*Bcat1*$^{-/-}$) and wild-type (WT) littermate mice were previously described (Ananieva et al., 2014) and maintained according to protocols approved by the University of Virginia Animal Care and Use Committee. To rederive *Slc40a*$^{flox/flox}$ mice, sperm from conditional-ready heterozygous *Slc40a1*-floxed mice (C57BL/6N-Slc40a1$^{tm1c(EUCOMM)Hmgu/H}$) was obtained from MRC Harwell and used for *in vitro* fertilisation of

C57BL/6N female mice. LysM-Cre mice (Lyz2$^{tm1(cre)Ifo}$) were obtained from The Jackson Laboratory. *Slc40a1*$^{flox/flox}$ and LysM-Cre mice were crossed to generate *Slc40a1*$^{\Delta LysMCre}$ mice in which *Slc40a1* is deleted in cells of the monocyte-macrophage-osteoclast lineage. *Slc40a1*$^{flox/flox}$ littermates were used as controls in all experiments. All animals were housed in standard caging on a 12-hr-light cycle and provided with free access to chow and water.

Tissues were collected and placed in either 70% ethanol or 10% neutral buffered formalin for 24 h prior to storage in 70% ethanol. Samples were randomly assigned to batches for rapid-throughput analysis. All studies were performed in accordance to the U.K. Animal (Scientific Procedures) Act 1986, the ARRIVE guidelines, the EU Directive 2010/63/EU for animal experiments and practices prescribed by the National Institutes of Health in the United States.

The International Mouse Phenotyping Consortium (IMPC: http://www.mousephenotype.org) and the International Knockout Mouse Consortium (IKMC) are generating null alleles for all protein-coding genes in mice on a C57BL/6 genetic background (International Mouse Knockout et al., 2007). The Origins of Bone and Cartilage Disease Programme (OBCD) is undertaking a validated rapid-throughput multiparameter skeletal phenotype screen (Bassett et al., 2012a; Freudenthal et al., 2016) of mutant mouse lines generated by the Wellcome Trust Sanger Institute as part of the IKMC and IMPC effort.

Digital X-ray microradiography

Femurs and caudal vertebrae 6 and 7 from 16 week-old mice and 14 week-old rats were fixed in 70% ethanol. Soft tissue was removed and digital X-ray images were recorded at 10 µm pixel resolution using a Faxitron MX20 variable kV point projection X-ray source and digital image system (Qados, Cross Technologies plc, UK) operating at 26 kV and 5x magnification. Bone mineral content (BMC) was determined relative to steel, aluminium and polyester standards as described (Bassett et al., 2012b). Images were calibrated with a

digital micrometre and bone and vertebra length was determined (Bassett et al., 2012a; Bassett et al., 2012b).

Micro-computerised tomography (micro-CT)

Mouse and rat femurs were analysed by micro-CT (Scanco uCT50, 70 kV, 200 µA, 0.5-mm aluminium filter) as described (Bassett et al., 2012a). Measurements included cortical bone parameters (cortical thickness (Ct.Th), cortical bone mineral density (Ct.BMD), internal diameter (Int.Dia) and bone area (Ct.Ar) at 10µm^3 voxel resolution in a 1.5mm^2 region centred on the mid-shaft region 56% of the way along the length of the femur distal to the femoral head, and trabecular parameters (bone volume (BV/TV), trabecular number (Tb.N), thickness (Tb.Th), spacing (Tb.Sp), structure model index (SMI) and trabecular BMD (Tb.BMD)) at 5µm^3 voxel resolution in a 1mm^2 region beginning 100µm proximal to the distal growth plate. Parameters were determined using Scanco analysis software.

Destructive 3-point bend testing

Destructive 3-point bend tests were performed on femurs and compression tests on caudal vertebrae 6 and 7 using an Instron 5543 load frame and load cell (100N for mouse femurs and 500N for mouse caudal vertebrae and rat bones) (Instron Limited, High Wycombe, Buckinghamshire, UK) as described (Bassett et al., 2012a). Bones were positioned horizontally on custom supports and load was applied perpendicular to the mid-diaphysis with a constant rate of displacement of 0.03 mm/s until fracture. Vertebrae were bonded in vertical alignment to a custom anvil support using cyanoacrylate glue and load was applied vertically at a constant rate of displacement of 0.03 mm/s and a sample rate of 20 Hz. Yield load, maximum load, fracture load, stiffness and toughness (Energy dissipated prior to fracture) were determined from femur load displacement curves and yield load, maximum load and stiffness from caudal vertebrae load displacement curves..

Osteoclast histomorphometry

Osteoclast numbers were determined according to the American Society for Bone and Mineral Research system (Dempster et al., 2013) in paraffin sections from decalcified mouse femurs stained for tartrate resistant acid phosphatase (TRAP) activity, counterstained with aniline blue and imaged using a Leica DM LB2 microscope and DFC320 digital camera (Bassett et al., 2014). A montage of nine overlapping fields covering an area of 1mm^2 located 0.2mm below the growth plate was constructed for each bone. BV/TV was measured, and osteoclast numbers and surface were determined in trabecular bone normalised to total bone surface (Bassett et al., 2014).

Cell culture, transfection and assessment of cell multinucleation

Human monocyte-derived macrophages were separated from healthy donor buffy coats by centrifugation through a Histopaque 1077 (Sigma) gradient and adhesion purification. Following Histopaque separation, peripheral blood mononuclear cells were re-suspended in RPMI (Life Technologies) and monocytes purified by adherence for 1 h at 37 °C, 5% CO_2 in twelve-well plates. The monolayer was washed 3 times with HBSS to remove non-adherent cells and monocytes were differentiated for 3 days in RPMI media containing 20 ng/ml M-CSF and 20 ng/ml recombinant human RANKL (PeproTech, UK). After 3 days of culture, cells were transfected using Dharmafect 1 (Dharmacon) diluted 1:50 in OPTIMEM medium (Invitrogen). siGENOME SMARTpools (100 nM, Dharmacon SMART pool) targeting human *APPL2*, *ATP8B2*, *BCAT1*, *DEPTOR*, *DOT1L*, *EGFR*, *EML1*, *EPS15*, *IGSF8*, *PIK3CB*, *RNF125*, *SLC1A4* and *SLC40A1* were used for RNAi and a non-targeting siRNA pool was used as the scrambled control siRNA. Primer sequence information is available in Supplementary Material 1. At the end of the culture, cells were fixed in formalin and stained for TRAP. The number of TRAP-positive cells with > 4 nuclei was normalised to the total number of cells in the field.

Quantitative RT-PCR

For quantitative RT-PCR (RT-qPCR), total RNA was extracted from human osteoclasts using the TRIzol reagent (Invitrogen, Carlsbad, CA) according to the manufacturer's instructions. Complementary DNA (cDNA) was synthesised using iScript cDNA Synthesis Kit (Bio-Rad, Hercules, CA). A total of 10ng cDNA for each sample was used and all RT-qPCR reactions were performed on a ViaA 7 Real-Time PCR System (Life Technologies, Carlsbad, CA) using Brilliant II SYBR Green QPCR Master Mix (Agilent, Santa Clara, CA). Results were analysed by the comparative Ct method using ViiA 7 RUO software, and each sample was normalised relative to *HPRT* expression.

***In vitro* resorption**

In vitro resorption activity of human osteoclasts was measured on Osteo Assay Surface 96 well plates (Corning). siRNA transfected cells were incubated with cell dissociation buffer (Sigma) and 10^5 cells/well were seeded in Osteo Assay Surface Plates. After 2 days of culture with 20 ng/ml M-CSF and 20 ng/ml recombinant human RANKL (PeproTech, UK), the wells were rinsed twice with PBS and incubated with 10% bleach solution for 30 min at room temperature. The wells were then washed twice with PBS and allowed to dry at room temperature. Individual resorption pits were imaged by light microscopy. Images were inverted and processed using Photoshop to yield high-contrast images and show the resorbed areas in black against a white background. Binary images of each individual well were then subjected to automated analysis (ImageJ), using constant "threshold" and "minimum particle" levels, to determine the number and surface area of resorbed pits.

Statistical analysis

Data are presented as mean ± standard deviations (SD) and analysed using GraphPad Prism software (version 7.02; GraphPad). Normally distributed data were analysed by 2 tailed Student's t test. Relationships between micro-CT parameters and *in vitro* osteoclastogenesis were determined by Pearson correlation. Frequency distributions of bone mineral densities obtained by x-ray microradiography were compared using the Kolmogorov-

Smirnov test. Differences in percentage of control following si-RNA knockdown in primary osteoclasts were tested for significance using a one-sample-t test.

IMPC mutant lines were compared to C57BL6/J strain-specific reference ranges that have been established for all parameters using 16 week-old female wild-type mice (n=320) obtained from control cohorts. Strains in which a structural or functional parameter was ±2.0 SD from the C57BL6/J reference mean were considered as outliers.

The hypergeometric test was used to determine whether the MMnet network (n=190 rat genes, of which 178 genes had a unique human orthologue) was enriched for genes with a GWAS signal ($P<10^{-6}$) for traits related to bone and height (Table 1) in the NHGRI-EBI Catalog of published GWAS (https://www.ebi.ac.uk/gwas/). Over-representation of GWAS gene signals in MMnet was assessed in comparison with the whole set of eQTLs (n=1,527 genes, of which 1,448 genes had a unique human orthologue) that were previously mapped in multinucleating macrophages (Kang et al., 2014). Biomart was used to map rat genes to the human orthologues (one-to-one orthology) using Ensembl rel. 98.

Results

MMnet regulates adult bone homeostasis via control of osteoclast multinucleation

MMnet is a co-expression network comprising 190 osteoclast-enriched eQTLs that are regulated in *trans* by *Trem2* (Kang et al., 2014). It was generated by using primary macrophages from a heterogenous rat population derived from experimental crossing of inbred Wistar Kyoto (WKY) and LEW rats. Macrophages from WKY rats display spontaneous fusion and multinucleation, whereas spontaneous macrophage fusion does not occur in Lewis (LEW) rats (Kang et al., 2014). Since macrophage fusion and multinucleation are essential for osteoclast function (Pereira et al., 2018), we reasoned that WKY and LEW rats would exhibit divergent skeletal phenotypes. Skeletal phenotype analysis demonstrated that, compared to LEW rats, WKY rats have decreased bone length accompanied by low bone mineral content (BMC), decreased trabecular bone volume (BV/TV) and thickness

(Tb.Th), together with reduced cortical bone thickness (Ct.Th) and mineral density (BMD). These abnormalities resulted in markedly decreased bone strength (Figure S1). Overall, these data indicate that spontaneous macrophage and osteoclast multinucleation in WKY rats is associated with low bone mass, mineralisation and strength. Thus, these findings suggest that MMnet regulates adult bone homeostasis via its action in osteoclasts to control multinucleation.

MMnet genes are enriched in human skeletal GWAS

To investigate further, we first determined whether MMnet eQTL genes are significantly enriched for GWAS loci associated with bone disorders in humans. In comparison with the background set of eQTLs (1,448 eQTLs that were previously mapped in multinucleating macrophages (Kang et al., 2014), MMnet was generally enriched for bone-related GWAS loci (P=0.0085, hypergeometric test, Table 1) and more specifically for heel bone mineral density associated GWAS variants (Table 1 and S1), which had the most significant enrichment (20 loci, P=4.49x10^{-3}, hypergeometric test, Table 1). Consistent with the decreased bone length observed in WKY rats, MMnet was also significantly enriched for body height variants (24 loci, P=1.86x10^{-2}, hypergeometric test, Table 1). In addition to enrichment for GWAS loci associated with skeletal traits, 9 MMnet genes have also been implicated in the pathogenesis of rare monogenic skeletal disorders (*CTSK*, *FAM20C*, *FLNA*, *FN1*, *IDUA*, *IL1RN*, *MANBA*, *MET*, *MMP9*) (Mortier et al., 2019). These results demonstrate that MMnet is conserved in humans and implicated in the regulation of skeletal development and bone homeostasis.

BCAT1 maintains normal bone mass and strength by regulating osteoclast multinucleation and function

To validate the role of MMnet, we investigated the effect of the MMnet hub gene *Bcat1* on osteoclast multinucleation and resorption, and bone mass (Figure 1A). 12 week-old male *Bcat1*$^{-/-}$ mice had high bone mass characterised by increased cortical thickness (Ct.Th),

trabecular bone volume (BV/TV), number (Tb.N) and thickness (Tb.Th), and reduced trabecular separation (Tb.Sp) and structural model index (SMI) (n=8 per genotype) (Figure 1B-C, S2). Biomechanical 3-point bend testing demonstrated that *Bcat1*$^{-/-}$ mice had enhanced bone strength characterised by increased yield, maximum and fracture loads and stiffness (Figure 1B-C, S2). Furthermore, static histomorphometry showed that *Bcat1*$^{-/-}$ mice had decreased osteoclast surface (Oc.S/BS) and number (Oc.N/BS), suggesting their high bone mass phenotype results from impaired osteoclast activity (Figure 1D). Consistent with this, siRNA-mediated knockdown of *BCAT1* expression in human osteoclasts *in vitro* inhibited multinucleation and resorption by 60%. By comparison, knockdown of *DCSTAMP*, a known master regulator of osteoclast and macrophage membrane fusion (Yagi et al., 2005; Yagi et al., 2006), resulted in 90% inhibition of osteoclast multinucleation and resorption (Figure 1E and F). Taken together, these data demonstrate an important new role for BCAT1 in osteoclast formation and function, and in the physiological maintenance of adult bone mass and strength.

MMnet genes have counter regulatory roles in the maintenance of adult bone mass and strength

To investigate whether individual MMnet genes regulate skeletal homeostasis, we studied all the MMnet genes for which the Wellcome Trust Sanger Institute, as part of the IMPC, had generated KO mice. Rapid-throughput phenotyping (Bassett et al., 2012a; Estrada et al., 2012; Kemp et al., 2017; Kim, 2018; Medina-Gomez et al., 2018; Morris et al., 2019) of samples from 16 week-old female mice with deletion of 12 MMnet genes (*Appl2*$^{-/-}$, *Atp8b2*$^{+/-}$, *Deptor*$^{-/-}$, *Dot1l*$^{+/-}$, *Egfr*$^{+/-}$, *Eml1*$^{-/-}$, *Eps15*$^{-/-}$, *Igsf8*$^{-/-}$, *Pik3cb*$^{-/-}$, *Rnf125*$^{-/-}$, *Slc1a4*$^{-/-}$, *Tgfb1i1*$^{-/-}$ mice) was performed using X-ray microradiography, micro-CT and biomechanical testing (Figure 2A). Six of the 12 MMnet KO mouse lines exhibited abnormal skeletal phenotypes, whereas *Dot1l*$^{+/-}$, *Egfr*$^{+/-}$, *Eps15*$^{-/-}$, *Rnf125*$^{-/-}$, *Slc1a4*$^{-/-}$ and *Tgfb1i1*$^{-/-}$ mice displayed no skeletal abnormalities (Figure 2B). *Igsf8*$^{-/-}$ mice had decreased femur length (Table S2); *Pik3cb*$^{-/-}$ (increased BV/TV and Tb.N), *Appl2*$^{-/-}$ (increased BV/TV) and *Atp8b2*$^{+/-}$ (increased BV/TV)

mice had high bone mass; whereas *Deptor*$^{-/-}$ (decreased BV/TV and Tb.N) mice had low bone mass (Figure 2C-D, Table S2). Biomechanical testing demonstrated decreased bone strength in *Atp8b2*$^{+/-}$ (decreased femur stiffness), *Deptor*$^{-/-}$ (decreased vertebral stiffness) and *Eml1*$^{-/-}$ (decreased vertebral stiffness) mice (Figure 2E-F, Table S2).

Human MMnet orthologues regulate osteoclast multinucleation and resorption

To investigate whether the divergent skeletal phenotypes identified in MMnet knockout mice correlate with osteoclast multinucleation and resorption *in vitro*, we determined the functional consequences of siRNA-mediated knockdown of 11 human orthologues of these MMnet genes in human osteoclasts (*TGFB1I1* was not expressed). The MMnet gene *DCSTAMP* was included as a positive control (Figure 3A and S3A). Knockdown of the 11 orthologous MMnet genes did not affect cell viability and resulted in greater than 80% inhibition of MMnet gene mRNA expression (Figure S3B-C). The functional consequences of *in vitro* siRNA knockdown correlated with the skeletal consequences of gene deletion *in vivo* (Figure 3B-D). Knockdown of *DOTL1*, *EPS15* and *RNF125* had no effect on osteoclast multinucleation or resorption and the skeletal phenotype of the corresponding knockout mice was also unaffected. Furthermore, knockdown of *APPL2* inhibited osteoclast resorption and knockdown of *PIK3CB* and *ATP8B2* inhibited both multinucleation and resorption whilst the corresponding knockout mice displayed increased bone mass. By contrast, knockdown of *DEPTOR* resulted in a marked stimulation of both multinucleation and resorption, and *DEPTOR* deficient mice had reduced bone mass and vertebral stiffness. Overall, the effects of mRNA knockdown of MMnet genes on *in vivo* osteoclast multinucleation and resorption were concordant and strongly correlated (R^2 = 0.76; P <0.001) (Figure 3E). Moreover, the effect of knockdown of MMnet genes on osteoclast resorption was also strongly and inversely correlated with trabecular bone mass (BV/TV) in knockout mice (R^2 = 0.65; P <0.01) (Figure 3F).

These findings demonstrate that the effects of MMnet gene deletion on the skeletal phenotype of knockout mice result, at least in part, from the direct consequences of gene

deletion on osteoclast multinucleation and function, and that MMnet contains genes with important counter regulatory roles in the physiological control of adult bone mass and strength.

MMnet regulates bone mass and strength via direct actions in the macrophage-osteoclast lineage

MMnet contains 190 genes, of which 178 are annotated, and among these genes there are known regulators of osteoclast multinucleation (*Dcstamp*, *Mmp9*, *Ctsk*) but the majority of MMnet genes require further investigation. To determine if MMnet genes regulate adult bone mass and strength by direct actions in osteoclasts we developed a prioritisation pipeline to identify a novel and tractable MMnet gene to target for cell specific gene deletion in the macrophage-osteoclast cell lineage. To identify potential novel and tractable candidates we applied a bespoke *in silico* filtering to the 178 annotated MMnet genes. The following criteria were used as a stepwise prioritisation filter (Table S3): (i) conserved expression in human osteoclasts; (ii) conserved expression in mouse macrophages; (iii) unknown function in osteoclastogenesis (Pubmed, accessed December 2017); (iv) availability of the mouse model (http://www.informatics.jax.org/); (v) strength of the MMnet eQTL (R^2>1) (Kang et al., 2014); (vi) Membrane receptors with pharmacologically tractable signalling pathways (Figure S4A, Table S3). This prioritisation process identified five candidate MMnet genes (*FGR*, *LAT2*, *MYOF*, *FCGRT*, and *SLC40A1*) (Figure S4A-B). To identify the most robust regulator of osteoclast multinucleation we determined the consequences of siRNA-mediated knockdown of these five genes in human osteoclasts. Knockdown of all five MMnet genes resulted in greater than 80% inhibition of gene mRNA expression and greater than 40% inhibition of multinucleation (Figure S4C). Most strikingly, knockdown of *SLC40A1* (encoding the mammalian iron transporter, ferroportin) resulted in more than 80% inhibition of multinucleation, an effect comparable with that of the master regulator *DCSTAMP* (Figure S4C-D).

Consequently, SLC40A1 was prioritised for further investigation and we generated a myeloid lineage-specific knockout of *Slc40a1* by crossing *Slc40a1*$^{flox/flox}$ mice with LysM-cre mice. Femurs from 16 week-old male and female mutant *Slc40a1*$^{\Delta LysMCre}$ and control *Slc40a1*$^{flox/flox}$ mice were analysed by X-ray-microradiography, microCT and 3-point bend testing (n=8 per sex per genotype) (Figure 4 and Figure S5). *Slc40a1*$^{\Delta LysMCre}$ mice had greatly increased bone mass characterised by increased BMC (Figure 4B-C), cortical thickness (Ct.Th), trabecular BV/TV, Tb.N and Tb.Th compared to littermate controls (P<0.001). This high bone mass phenotype was associated with markedly increased bone strength characterised by increased yield, maximum and fracture loads (Figure 4C-D and Figure S5A-D). Consistent with this, histomorphometic analysis demonstrated decreased osteoclast surfaces (Oc.S/BS) in *Slc40a1*$^{\Delta LysMCre}$ mice (Figure 4F) and siRNA-mediated knockdown of *SLC40A1* expression, in human osteoclasts *in vitro,* inhibited osteoclast resorption by more than 85% (Figure 4G-H). Taken together, these data demonstrate that the MMnet gene, *Slc40a1,* acts as an important determinant of adult bone mass and strength by directly regulating osteoclast multinucleation and function.

Discussion

In this study, we took advantage of an unique *trans*-eQTL network (MMnet) in multinucleating rat primary macrophages that is enriched for osteoclast genes. The parental rat strains used to generate MMnet (WKY and LEW) had opposing skeletal phenotypes. Spontaneous fusion of WKY macrophages *in vitro* was associated with reduced bone length, mass, and strength *in vivo*, suggesting that genetic determinants of osteoclast multinucleation directly affect bone development and maintenance. These results implicate MMnet in the physiological regulation of adult bone mass and strength.

Next, we determined whether MMnet is enriched for GWAS variants associated with skeletal traits and showed enrichment for heel bone mineral density, body height, osteoarthritis and

384 psoriatic arthritis. These results confirm conservation of MMnet in humans and demonstrate
385 associations between MMnet and osteoclast multinucleation and bone mass. Furthermore,
386 the association of MMnet with osteoarthritis suggests involvement of osteoclasts in articular
387 cartilage degradation, an area that is gaining increasing attention (Goldring and Goldring,
388 2016; Lofvall et al., 2018).

389 To validate the function of MMnet *in vivo* we first investigated the role of the hub gene,
390 branched chain amino acid transferase 1 (*Bcat1*) in knockout mice and demonstrated
391 important new roles for BCAT1 in osteoclast formation and function, and the physiological
392 maintenance of adult bone mass and strength. These results demonstrate that MMnet has a
393 critical homeostatic role in bone that is conserved in rodents and humans. Furthermore, they
394 specifically implicate branched chain amino acid (BCAA) metabolism in osteoclast-mediated
395 bone homeostasis and are consistent with our recent observation that osteoclast numbers
396 and severity of collagen-induced arthritis are also reduced following pharmacological
397 inhibition of BCAT1 in mice (Papathanassiu et al., 2017). BCAT1 activity controls
398 intracellular leucine, a known activator of mammalian target of rapamycin complex 1
399 (mTORC1) signalling (Ananieva et al., 2014), suggesting that MMnet may directly regulate
400 mTORC1-dependent bone homeostasis and inflammation via the hub gene *Bcat1*.

401 To investigate further the homeostatic roles of MMnet in the maintenance of adult bone
402 mass and strength, we analysed knockout mice with deletion of 12 unselected MMnet genes
403 and demonstrated significant outlier phenotypes in six of these lines, which include both
404 known *Pik3cb* (Gyori et al., 2014; Hall et al., 1995; Lee et al., 2002) and unknown (*Atp8b2*,
405 *Igsf8*, *Eml1*, *Appl2, and Deptor*) regulators of skeletal homeostasis. Deletion of *Pik3cb,*
406 *Appl2* and *Atp8b2* resulted in increased bone mass whereas deletion of *Deptor* resulted in
407 decreased bone mass and strength, suggesting MMnet represents a conserved and
408 complex homeostatic counter regulatory network that serves to optimise bone structure and
409 strength. Consistent with this, deletion of MMnet's strongest *trans*-eQTL *Kcnn4* results in

410 increased bone mass (Kang et al., 2014) as did deletion of the *Dcstamp,* the master
411 regulator of membrane fusion (Yagi et al., 2005).

412 Overall, these studies reveal a common molecular pathway within MMnet that regulates
413 osteoclast multinucleation and function as well as bone mass. Thus, at least four MMnet
414 genes (*Trem2*, *Bcat1*, *Pik3cb* and *Deptor*), that include the network master regulator (*Trem2)*
415 and network hub (*Bcat1)*, act within the Trem2-Pi3K-mTORC1 pathway (Ananieva et al.,
416 2014; Mossmann et al., 2018; Peterson et al., 2009; Ulland et al., 2017). mTORC1 protein
417 kinase comprises a complex of proteins that includes DEPTOR (Peterson et al., 2009), a
418 regulator of cell growth and metabolism that is essential for osteoclast formation (Indo et al.,
419 2013). While *Trem2* (Ulland et al., 2017), *Bcat1* (Ananieva et al., 2014) and *Pik3cb*
420 (Mossmann et al., 2018) are positive regulators of mTORC1, *Deptor* inhibits mTORC1
421 activity (Peterson et al., 2009). Significantly, the divergent effects of these genes on activity
422 of the mTORC1 signalling pathway correlate precisely with the effects of gene knockdown or
423 deletion on osteoclast multinucleation and function *in vitro* and on skeletal phenotype *in vivo*.
424 Thus, knockdown or deletion of *Bcat1* and *Pik3cb* results in decreased osteoclast
425 multinucleation and resorption, and increased bone mass, whereas knockdown or deletion of
426 *Deptor* results in opposite cellular and *in vivo* phenotypes. Together, these data suggest a
427 pivotal and integrated counter-regulatory role for the Trem2-Pi3K-mTORC1 pathway in
428 osteoclast multinucleation and function, and the homeostatic control of bone mass, and may
429 thus provide novel therapeutic targets for the inhibition of bone loss.

430 Finally, we investigated the role of the iron transporter ferroportin, encoded by the MMnet
431 gene *Slc40a1*, in the osteoclast lineage. Ferroportin was identified as a powerful inhibitor of
432 osteoclast multinucleation and function *in vitro*, with a potency equivalent to *Dcstamp*
433 (Figures 4 and S4). Generation of mice with conditional deletion of *Slc40a1* in the
434 macrophage-osteoclast lineage using *LysMCre* mice was consistent with *in vitro* data and
435 resulted in a phenotype of increased bone mass and strength (Figures 4 and S5). Thus,
436 *Slc40a1* regulates bone structure and strength via direct actions in the macrophage-

437 osteoclast lineage, further supporting the conclusion that MMnet plays a key role in the
438 physiological regulation of bone mass by osteoclasts.

439 Nevertheless, Wang and colleagues (Wang et al., 2018) recently reported that deletion of
440 *Slc40a1* in the macrophage-osteoclast lineage using *LysMCre* mice causes decreased bone
441 mass and mineralisation in female, but not male, mice. Wang *et al* also reported that
442 deletion of *Slc40a1* in terminally differentiated osteoclasts using *CtskCre* mice resulted in no
443 skeletal abnormalities in either sex. The discordance between our findings and those
444 reported by Wang *et al* may be due to differences in the age at which mice were phenotyped
445 and the strain of *Slc40a1* floxed mice investigated (*C57BL/6N-Slc40a1*$^{tm1c(EUCOMM)Hmgu/H}$ in
446 this study compared to *129S-Slc40a1*$^{tm2Nca/J}$ by Wang and colleagues). In *C57BL/6N-*
447 *Slc40a1*$^{tm1c(EUCOMM)Hmgu/H}$ mice exons 4 and 5 of *Slc40a1* are deleted in cre-expressing
448 tissues whereas in *129S-Slc40a1*$^{tm2Nca/J}$ exons 6 and 7 are deleted. Here, we demonstrate
449 a high bone mass phenotype with increased bone strength in adult male and female
450 *Slc40a1*$^{\Delta LysMCre}$ mice aged 16 weeks after acquisition of peak bone mass, whereas Wang *et*
451 *al* studied animals in the middle of the rapid growth period at 8 weeks of age, did not
452 investigate bone strength and only identified skeletal abnormalities in females. Although it is
453 clear that ferroportin acts directly in the macrophage-osteoclast lineage, further longitudinal
454 studies will be required to define its temporal effects on bone mass and strength, whilst
455 studies with the different floxed strains may be required to determine whether modifier genes
456 influence the skeletal response to deletion of *Slc40a1*.

457 Systems genetics studies use naturally occurring genetic variation to identify gene networks
458 that are associated with the trait of interest in disease-relevant cells (Baliga et al., 2017).
459 Systems genetic approaches in osteoblasts and osteoclasts have been previously carried
460 out to identify genes that are implicated in skeletal homeostasis (Calabrese et al., 2012;
461 Calabrese et al., 2017; Farber et al., 2011; Mesner et al., 2019; Mesner et al., 2014). Here,
462 we have used systems genetics approaches to demonstrate that a complex *trans*-eQTL
463 network (MMnet) facilitates homeostatic control of bone mass via its effects on osteoclast

fusion and function that are mediated in large part by the mTOR pathway. This physiologically important network is conserved in rats, mice and humans and its identification will lead the way to an understanding of the gene-gene interactions and network-based therapeutic approaches that may be used in osteoclast-mediated inflammatory disease or to prevent bone loss.

GWAS trait	Number of eQTLs genes (background) with at least one GWAS hit	Number of MMnet genes with at least one GWAS hit	Frequency (%) eQTLs genes (background) with at least one GWAS hit	Frequency (%) MMnet genes with at least one GWAS hit	P-value MMnet enrichment over background (hypergeometric test)
All GWAS combined	**299**	**41**	**20.3%**	**27.7%**	**0.0085**
Heel bone mineral density	**117**	**20**	**8.0%**	**13.5%**	**0.0045**
Osteoarthritis	**9**	**3**	**0.6%**	**2.0%**	**0.0083**
Psoriatic arthritis	**2**	**1**	**0.1%**	**0.7%**	**0.0101**
Body height	**165**	**24**	**11.2%**	**16.2%**	**0.0186**
Bone quantitative ultrasound measurement	4	1	0.3%	0.7%	0.0527
Bone density	16	3	1.1%	2.0%	0.0686
Hip bone mineral density	5	1	0.3%	0.7%	0.0821
Spine bone mineral density	7	1	0.5%	0.7%	0.1509
Bone fracture	3	0	0.2%	0.0%	0.2727
Ankylosing spondylitis	4	0	0.3%	0.0%	0.3460
Periodontitis	4	0	0.3%	0.0%	0.3460
Rheumatoid arthritis	15	1	1.0%	0.7%	0.4550
Adolescent idiopathic scoliosis	60	5	4.1%	3.4%	0.5723
Bone mineral content measurement	1	1	0.1%	0.7%	-
Lumbar disc degeneration	1	1	0.1%	0.7%	-
Osteitis deformans	1	0	0.1%	0.0%	-

Table 1. MMnet is significantly enriched for variants that associate with different bone traits. Single nucleotide polymorphisms (SNPs) significantly associated with the reported GWAS traits were interrogated in two datasets: the background dataset which includes all the eQTLs (posterior probability > 80% - see Methods) and MMnet gene set. The enrichment was then tested over the background using a hypergeometric test. The significant enriched traits are shown in bold.

ACKNOWLEDGEMENTS

We thank Mahrokh Nodani for technical assistance. We thank members of Sanger Mouse Pipelines (Mouse Informatics, Molecular Technologies, Genome Engineering Technologies, Mouse Production Team, Mouse Phenotyping) and the Research Support Facility for provision and management of mice. We thank Susan Hutson for providing the *Bcat1*$^{-/-}$ mice. This work was supported by the Medical Research Council 'Control of Macrophage Multinucleation in Health and Disease' (MR/N01121X/1 to JB, GRW, JHDB) and a Wellcome Trust Strategic Award (Grant Number 101123 to GRW and JHDB).

AUTHOR CONTRIBUTIONS

Conceptualisation: JB, GRW, JHDB; Methodology: MP, JB, GRW, JHDB, MR, EP, KSP; Investigation: MP, JHK, JL, KBK; Visualisation: MP, JB, GRW, JHDB; Supervision: JB, GRW, JHDB; Funding Acquisition: JB, GRW, JHDB; Writing – Original Draft: MP, JB; Writing – Review & Editing: MP, JB, GRW, JHDB, EP, KSP. All of the authors read and approved the final manuscript.

DECLARATIONS OF INTEREST

The authors declare no competing interests

References

Al-Barghouthi, B.M., and Farber, C.R. (2019). Dissecting the Genetics of Osteoporosis using Systems Approaches. Trends Genet *35*, 55-67.

Albagha, O.M., Visconti, M.R., Alonso, N., Langston, A.L., Cundy, T., Dargie, R., Dunlop, M.G., Fraser, W.D., Hooper, M.J., Isaia, G.*, et al.* (2010). Genome-wide association study identifies variants at CSF1, OPTN and TNFRSF11A as genetic risk factors for Paget's disease of bone. Nat Genet *42*, 520-524.

Albert, F.W., Bloom, J.S., Siegel, J., Day, L., and Kruglyak, L. (2018). Genetics of trans-regulatory variation in gene expression. Elife *7*.

Albert, F.W., and Kruglyak, L. (2015). The role of regulatory variation in complex traits and disease. Nat Rev Genet *16*, 197-212.

Ananieva, E.A., Patel, C.H., Drake, C.H., Powell, J.D., and Hutson, S.M. (2014). Cytosolic branched chain aminotransferase (BCATc) regulates mTORC1 signaling and glycolytic metabolism in CD4+ T cells. J Biol Chem *289*, 18793-18804.

Bagnati, M., Moreno-Moral, A., Ko, J.H., Nicod, J., Harmston, N., Imprialou, M., Game, L., Gil, J., Petretto, E., and Behmoaras, J. (2019). Systems genetics identifies a macrophage cholesterol network associated with physiological wound healing. JCI Insight *4*.

Bassett, J.H., Boyde, A., Zikmund, T., Evans, H., Croucher, P.I., Zhu, X., Park, J.W., Cheng, S.Y., and Williams, G.R. (2014). Thyroid hormone receptor alpha mutation causes a severe and thyroxine-resistant skeletal dysplasia in female mice. Endocrinology *155*, 3699-3712.

Bassett, J.H., Gogakos, A., White, J.K., Evans, H., Jacques, R.M., van der Spek, A.H., Sanger Mouse Genetics, P., Ramirez-Solis, R., Ryder, E., Sunter, D.*, et al.* (2012a). Rapid-throughput skeletal phenotyping of 100 knockout mice identifies 9 new genes that determine bone strength. PLoS Genet *8*, e1002858.

Bassett, J.H., van der Spek, A., Gogakos, A., and Williams, G.R. (2012b). Quantitative X-ray imaging of rodent bone by Faxitron. Methods in molecular biology *816*, 499-506.

Battle, A., Mostafavi, S., Zhu, X., Potash, J.B., Weissman, M.M., McCormick, C., Haudenschild, C.D., Beckman, K.B., Shi, J., Mei, R.*, et al.* (2014). Characterizing the genetic basis of transcriptome diversity through RNA-sequencing of 922 individuals. Genome Res *24*, 14-24.

Boyle, E.A., Li, Y.I., and Pritchard, J.K. (2017). An Expanded View of Complex Traits: From Polygenic to Omnigenic. Cell *169*, 1177-1186.

Brem, R.B., Yvert, G., Clinton, R., and Kruglyak, L. (2002). Genetic dissection of transcriptional regulation in budding yeast. Science *296*, 752-755.

Brynedal, B., Choi, J., Raj, T., Bjornson, R., Stranger, B.E., Neale, B.M., Voight, B.F., and Cotsapas, C. (2017). Large-Scale trans-eQTLs Affect Hundreds of Transcripts and Mediate Patterns of Transcriptional Co-regulation. Am J Hum Genet *100*, 581-591.

Calabrese, G., Bennett, B.J., Orozco, L., Kang, H.M., Eskin, E., Dombret, C., De Backer, O., Lusis, A.J., and Farber, C.R. (2012). Systems genetic analysis of osteoblast-lineage cells. PLoS Genet *8*, e1003150.

Calabrese, G.M., Mesner, L.D., Stains, J.P., Tommasini, S.M., Horowitz, M.C., Rosen, C.J., and Farber, C.R. (2017). Integrating GWAS and Co-expression Network Data Identifies Bone Mineral Density Genes SPTBN1 and MARK3 and an Osteoblast Functional Module. Cell Syst *4*, 46-59 e44.

Dempster, D.W., Compston, J.E., Drezner, M.K., Glorieux, F.H., Kanis, J.A., Malluche, H., Meunier, P.J., Ott, S.M., Recker, R.R., and Parfitt, A.M. (2013). Standardized nomenclature, symbols, and units for bone histomorphometry: a 2012 update of the report of the ASBMR Histomorphometry Nomenclature Committee. J Bone Miner Res *28*, 2-17.

DiCarlo, E.F., and Kahn, L.B. (2011). Inflammatory diseases of the bones and joints. Semin Diagn Pathol *28*, 53-64.

Estrada, K., Styrkarsdottir, U., Evangelou, E., Hsu, Y.H., Duncan, E.L., Ntzani, E.E., Oei, L., Albagha, O.M., Amin, N., Kemp, J.P.*, et al.* (2012). Genome-wide meta-analysis identifies 56

bone mineral density loci and reveals 14 loci associated with risk of fracture. Nat Genet *44*, 491-501.

Farber, C.R., Bennett, B.J., Orozco, L., Zou, W., Lira, A., Kostem, E., Kang, H.M., Furlotte, N., Berberyan, A., Ghazalpour, A.*, et al.* (2011). Mouse genome-wide association and systems genetics identify Asxl2 as a regulator of bone mineral density and osteoclastogenesis. PLoS Genet *7*, e1002038.

Fehrmann, R.S., Jansen, R.C., Veldink, J.H., Westra, H.J., Arends, D., Bonder, M.J., Fu, J., Deelen, P., Groen, H.J., Smolonska, A.*, et al.* (2011). Trans-eQTLs reveal that independent genetic variants associated with a complex phenotype converge on intermediate genes, with a major role for the HLA. PLoS Genet *7*, e1002197.

Freudenthal, B., Logan, J., Sanger Institute Mouse, P., Croucher, P.I., Williams, G.R., and Bassett, J.H. (2016). Rapid phenotyping of knockout mice to identify genetic determinants of bone strength. J Endocrinol *231*, R31-46.

Furlong, L.I. (2013). Human diseases through the lens of network biology. Trends Genet *29*, 150-159.

Galson, D.L., and Roodman, G.D. (2014). Pathobiology of Paget's Disease of Bone. J Bone Metab *21*, 85-98.

Goldring, S.R., and Goldring, M.B. (2016). Changes in the osteochondral unit during osteoarthritis: structure, function and cartilage-bone crosstalk. Nat Rev Rheumatol *12*, 632-644.

Grundberg, E., Small, K.S., Hedman, A.K., Nica, A.C., Buil, A., Keildson, S., Bell, J.T., Yang, T.P., Meduri, E., Barrett, A.*, et al.* (2012). Mapping cis- and trans-regulatory effects across multiple tissues in twins. Nat Genet *44*, 1084-1089.

Gyori, D., Csete, D., Benko, S., Kulkarni, S., Mandl, P., Dobo-Nagy, C., Vanhaesebroeck, B., Stephens, L., Hawkins, P.T., and Mocsai, A. (2014). The phosphoinositide 3-kinase isoform PI3Kbeta regulates osteoclast-mediated bone resorption in humans and mice. Arthritis Rheumatol *66*, 2210-2221.

Hall, T.J., Jeker, H., and Schaueblin, M. (1995). Wortmannin, a potent inhibitor of phosphatidylinositol 3-kinase, inhibits osteoclastic bone resorption in vitro. Calcif Tissue Int *56*, 336-338.

Heinig, M., Petretto, E., Wallace, C., Bottolo, L., Rotival, M., Lu, H., Li, Y., Sarwar, R., Langley, S.R., Bauerfeind, A.*, et al.* (2010). A trans-acting locus regulates an anti-viral expression network and type 1 diabetes risk. Nature *467*, 460-464.

Indo, Y., Takeshita, S., Ishii, K.A., Hoshii, T., Aburatani, H., Hirao, A., and Ikeda, K. (2013). Metabolic regulation of osteoclast differentiation and function. J Bone Miner Res *28*, 2392-2399.

International Mouse Knockout, C., Collins, F.S., Rossant, J., and Wurst, W. (2007). A mouse for all reasons. Cell *128*, 9-13.

Johnson, M.R., Behmoaras, J., Bottolo, L., Krishnan, M.L., Pernhorst, K., Santoscoy, P.L.M., Rossetti, T., Speed, D., Srivastava, P.K., Chadeau-Hyam, M.*, et al.* (2015). Systems genetics identifies Sestrin 3 as a regulator of a proconvulsant gene network in human epileptic hippocampus. Nat Commun *6*, 6031.

Kang, H., Kerloc'h, A., Rotival, M., Xu, X., Zhang, Q., D'Souza, Z., Kim, M., Scholz, J.C., Ko, J.H., Srivastava, P.K.*, et al.* (2014). Kcnn4 is a regulator of macrophage multinucleation in bone homeostasis and inflammatory disease. Cell Rep *8*, 1210-1224.

Kemp, J.P., Morris, J.A., Medina-Gomez, C., Forgetta, V., Warrington, N.M., Youlten, S.E., Zheng, J., Gregson, C.L., Grundberg, E., Trajanoska, K.*, et al.* (2017). Identification of 153 new loci associated with heel bone mineral density and functional involvement of GPC6 in osteoporosis. Nat Genet *49*, 1468-1475.

Kim, S.K. (2018). Identification of 613 new loci associated with heel bone mineral density and a polygenic risk score for bone mineral density, osteoporosis and fracture. PLoS One *13*, e0200785.

Lee, M.N., Ye, C., Villani, A.C., Raj, T., Li, W., Eisenhaure, T.M., Imboywa, S.H., Chipendo, P.I., Ran, F.A., Slowikowski, K.*, et al.* (2014). Common genetic variants modulate pathogen-sensing responses in human dendritic cells. Science *343*, 1246980.

606 Lee, S.E., Woo, K.M., Kim, S.Y., Kim, H.M., Kwack, K., Lee, Z.H., and Kim, H.H. (2002). The
607 phosphatidylinositol 3-kinase, p38, and extracellular signal-regulated kinase pathways are
608 involved in osteoclast differentiation. Bone *30*, 71-77.
609 Liu, J., Zhou, Y., Liu, S., Song, X., Yang, X.Z., Fan, Y., Chen, W., Akdemir, Z.C., Yan, Z.,
610 Zuo, Y.*, et al.* (2018). The coexistence of copy number variations (CNVs) and single
611 nucleotide polymorphisms (SNPs) at a locus can result in distorted calculations of the
612 significance in associating SNPs to disease. Hum Genet *137*, 553-567.
613 Liu, X., Li, Y.I., and Pritchard, J.K. (2019). Trans Effects on Gene Expression Can Drive
614 Omnigenic Inheritance. Cell *177*, 1022-1034 e1026.
615 Lofvall, H., Newbould, H., Karsdal, M.A., Dziegiel, M.H., Richter, J., Henriksen, K., and
616 Thudium, C.S. (2018). Osteoclasts degrade bone and cartilage knee joint compartments
617 through different resorption processes. Arthritis Res Ther *20*, 67.
618 Manolagas, S.C. (2010). From estrogen-centric to aging and oxidative stress: a revised
619 perspective of the pathogenesis of osteoporosis. Endocrine reviews *31*, 266-300.
620 McInnes, I.B., and Schett, G. (2011). The pathogenesis of rheumatoid arthritis. The New
621 England journal of medicine *365*, 2205-2219.
622 Medina-Gomez, C., Kemp, J.P., Trajanoska, K., Luan, J., Chesi, A., Ahluwalia, T.S., Mook-
623 Kanamori, D.O., Ham, A., Hartwig, F.P., Evans, D.S.*, et al.* (2018). Life-Course Genome-
624 wide Association Study Meta-analysis of Total Body BMD and Assessment of Age-Specific
625 Effects. Am J Hum Genet *102*, 88-102.
626 Mesner, L.D., Calabrese, G.M., Al-Barghouthi, B., Gatti, D.M., Sundberg, J.P., Churchill,
627 G.A., Godfrey, D.A., Ackert-Bicknell, C.L., and Farber, C.R. (2019). Mouse genome-wide
628 association and systems genetics identifies Lhfp as a regulator of bone mass. PLoS Genet
629 *15*, e1008123.
630 Mesner, L.D., Ray, B., Hsu, Y.H., Manichaikul, A., Lum, E., Bryda, E.C., Rich, S.S., Rosen,
631 C.J., Criqui, M.H., Allison, M.*, et al.* (2014). Bicc1 is a genetic determinant of
632 osteoblastogenesis and bone mineral density. J Clin Invest *124*, 2736-2749.
633 Morley, M., Molony, C.M., Weber, T.M., Devlin, J.L., Ewens, K.G., Spielman, R.S., and
634 Cheung, V.G. (2004). Genetic analysis of genome-wide variation in human gene expression.
635 Nature *430*, 743-747.
636 Morris, J.A., Kemp, J.P., Youlten, S.E., Laurent, L., Logan, J.G., Chai, R.C., Vulpescu, N.A.,
637 Forgetta, V., Kleinman, A., Mohanty, S.T.*, et al.* (2019). An atlas of genetic influences on
638 osteoporosis in humans and mice. Nat Genet *51*, 258-266.
639 Mortier, G.R., Cohn, D.H., Cormier-Daire, V., Hall, C., Krakow, D., Mundlos, S., Nishimura,
640 G., Robertson, S., Sangiorgi, L., Savarirayan, R.*, et al.* (2019). Nosology and classification of
641 genetic skeletal disorders: 2019 revision. Am J Med Genet A *179*, 2393-2419.
642 Mossmann, D., Park, S., and Hall, M.N. (2018). mTOR signalling and cellular metabolism
643 are mutual determinants in cancer. Nat Rev Cancer *18*, 744-757.
644 Papathanassiu, A.E., Ko, J.H., Imprialou, M., Bagnati, M., Srivastava, P.K., Vu, H.A., Cucchi,
645 D., McAdoo, S.P., Ananieva, E.A., Mauro, C.*, et al.* (2017). BCAT1 controls metabolic
646 reprogramming in activated human macrophages and is associated with inflammatory
647 diseases. Nat Commun *8*, 16040.
648 Pereira, M., Petretto, E., Gordon, S., Bassett, J.H.D., Williams, G.R., and Behmoaras, J.
649 (2018). Common signalling pathways in macrophage and osteoclast multinucleation. J Cell
650 Sci *131*.
651 Peterson, T.R., Laplante, M., Thoreen, C.C., Sancak, Y., Kang, S.A., Kuehl, W.M., Gray,
652 N.S., and Sabatini, D.M. (2009). DEPTOR is an mTOR inhibitor frequently overexpressed in
653 multiple myeloma cells and required for their survival. Cell *137*, 873-886.
654 Schadt, E.E., Monks, S.A., Drake, T.A., Lusis, A.J., Che, N., Colinayo, V., Ruff, T.G.,
655 Milligan, S.B., Lamb, J.R., Cavet, G.*, et al.* (2003). Genetics of gene expression surveyed in
656 maize, mouse and man. Nature *422*, 297-302.
657 Small, K.S., Hedman, A.K., Grundberg, E., Nica, A.C., Thorleifsson, G., Kong, A.,
658 Thorsteindottir, U., Shin, S.Y., Richards, H.B., Consortium, G.*, et al.* (2011). Identification of
659 an imprinted master trans regulator at the KLF14 locus related to multiple metabolic
660 phenotypes. Nat Genet *43*, 561-564.

661 Sobacchi, C., Schulz, A., Coxon, F.P., Villa, A., and Helfrich, M.H. (2013). Osteopetrosis:
662 genetics, treatment and new insights into osteoclast function. Nat Rev Endocrinol *9*, 522-
663 536.
664 Stahl, E.A., Raychaudhuri, S., Remmers, E.F., Xie, G., Eyre, S., Thomson, B.P., Li, Y.,
665 Kurreeman, F.A., Zhernakova, A., Hinks, A.*, et al.* (2010). Genome-wide association study
666 meta-analysis identifies seven new rheumatoid arthritis risk loci. Nat Genet *42*, 508-514.
667 Trajanoska, K., Morris, J.A., Oei, L., Zheng, H.F., Evans, D.M., Kiel, D.P., Ohlsson, C.,
668 Richards, J.B., Rivadeneira, F., consortium, G.G.*, et al.* (2018). Assessment of the genetic
669 and clinical determinants of fracture risk: genome wide association and mendelian
670 randomisation study. BMJ *362*, k3225.
671 Ulland, T.K., Song, W.M., Huang, S.C., Ulrich, J.D., Sergushichev, A., Beatty, W.L., Loboda,
672 A.A., Zhou, Y., Cairns, N.J., Kambal, A.*, et al.* (2017). TREM2 Maintains Microglial Metabolic
673 Fitness in Alzheimer's Disease. Cell *170*, 649-663 e613.
674 Wang, L., Fang, B., Fujiwara, T., Krager, K., Gorantla, A., Li, C., Feng, J.Q., Jennings, M.L.,
675 Zhou, J., Aykin-Burns, N.*, et al.* (2018). Deletion of ferroportin in murine myeloid cells
676 increases iron accumulation and stimulates osteoclastogenesis in vitro and in vivo. J Biol
677 Chem *293*, 9248-9264.
678 Wright, F.A., Sullivan, P.F., Brooks, A.I., Zou, F., Sun, W., Xia, K., Madar, V., Jansen, R.,
679 Chung, W., Zhou, Y.H.*, et al.* (2014). Heritability and genomics of gene expression in
680 peripheral blood. Nat Genet *46*, 430-437.
681 Yagi, M., Miyamoto, T., Sawatani, Y., Iwamoto, K., Hosogane, N., Fujita, N., Morita, K.,
682 Ninomiya, K., Suzuki, T., Miyamoto, K.*, et al.* (2005). DC-STAMP is essential for cell-cell
683 fusion in osteoclasts and foreign body giant cells. J Exp Med *202*, 345-351.
684 Yagi, M., Miyamoto, T., Toyama, Y., and Suda, T. (2006). Role of DC-STAMP in cellular
685 fusion of osteoclasts and macrophage giant cells. J Bone Miner Metab *24*, 355-358.
686 Yao, C., Joehanes, R., Johnson, A.D., Huan, T., Liu, C., Freedman, J.E., Munson, P.J., Hill,
687 D.E., Vidal, M., and Levy, D. (2017). Dynamic Role of trans Regulation of Gene Expression
688 in Relation to Complex Traits. Am J Hum Genet *100*, 985-986.

689

690

691

Figure legends

Figure 1. ***Bcat1*** **deficiency results in high bone mass due to decreased osteoclast fusion. (A)** Location of *Bcat1* in the MMnet hub (left panel)**.** Skeletal phenotyping of *Bcat1*$^{-/-}$ mice using X-ray microradiography, micro computed tomography (micro-CT) and 3 point bending testing (right panel). **(B)** Micro-CT images of distal femur trabecular bone and mid-diaphysis cortical bone in *Bcat1*$^{+/+}$ (wild-type, WT) and *Bcat1*$^{-/-}$ mice (upper panel) (scale bar = 200 µm). Trabecular bone volume/tissue volume (BV/TV) and cortical thickness (Ct.Th) are shown in the lower panel; n = 8 mice per genotype. **(C)** Representative load displacement curves from femur three-point bend testing (upper panel). Fracture load and stiffness are shown in the lower panel; n = 8 mice per genotype **(D)** Representative tartrate-resistant acid phosphatase (TRAP) stained sections from the proximal humerus of WT and *Bcat1*$^{-/-}$ mice showing osteoclasts in red (left panel). Quantification of the osteoclast surface/bone surface (Oc.S/BS) and osteoclast number/bone surface (N.Oc/BS) (right panel); n = 4 mice per genotype (scale bar = 100µm). **(E)** Representative images of TRAP+ multinucleated osteoclasts (upper panel) (scale bar = 40µm) and hydroxyapatite resorption (lower panel) (scale bar = 1mm) 2 days after siRNA transfection. **(F)** Percentage inhibition of multinucleation compared to scrambled siRNA (left panel) and percentage inhibition of hydroxyapatite resorption compared to scrambled siRNA (right panel); (Mean±SD from n=4 donors, **P*<0.05, ***P*<0.01, ****P*<0.001 vs scrambled siRNA, one-sample-t test).

Figure 2. MMnet regulates bone mass. (A) The location of the 12 MMnet genes for which knockout mice were available are highlighted in the network. **(B)** Venn diagram showing mutant strains with outlier phenotypes for bone mass, bone strength and bone length. **(C)** Representative micro-CT images of distal femur trabecular bone and mid diaphyseal cortical bone from WT and mutant mice (scale bar = 200 µm). **(D)** Graphs show trabecular bone volume (BV/TV), trabecular number (Tb.N) and trabecular separation (Tb.Sp). Grey box represents WT reference mean +/- 2SD (n= 320, 16 week old, female C57BL/6 WT mice). **(E)** Femur stiffness (Fem.stiffness) and vertebral stiffness (vert.stiffness). **(F)** Representative

load displacement curves for femur three-point bend testing and vertebral compression .Data from individual mice are shown as black dots and mean value by a red line (n = 2 or 6 per genotype). Parameters outside the WT reference rage are indicated by an asterisk *.

Figure 3. MMnet regulates human osteoclast multinucleation and resorption *in vitro*. **(A)** The location of the 11 MMnet genes for which knockout mice were available, and for which there are human homologs. The master regulator of macrophage fusion *Dcstamp* is highlighted in red. **(B)** Representative images of TRAP+ osteoclasts (Top panel) and hydroxyapatite resorption (Bottom panel) following si-RNA knockdown for *DCSTAMP*, *PIK3CB*, *ATP8B2*, *APPL2* and *DEPTOR.* **(C)** Graphs show the inhibition of multinucleation following si-RNA knockdown compared to scramble si-RNA control; n=4 donors (scale bar = 40µm). **(D)** Graphs show inhibition of hydroxyapatite resorption following si-RNA knockdown compared to scramble si-RNA control; n=4 donors (scale bar = 1mm). **(E)** Graph shows Pearson correlation between human osteoclast multinucleation and resorptive activity following si-RNA knockdown of 12 MMnet genes (R^2=0.76; *P*<0.001) **(F)** Graph shows Pearson correlation between human osteoclast resorption activity following si-RNA knockdown of 11 MMnet genes and BV/TV in the corresponding 11 MMnet knockout mouse strains (R^2 =0.65; *P*<0.01)**.** (Mean±SD from n=4 donors, **P*<0.05, ***P*<0.01, ****P*<0.001 vs scrambled siRNA, one-sample-t test).

Figure 4. **Myeloid-specific deletion of *Ferroportin* results in increased bone mass and strength due to impaired osteoclast multinucleation and function. (A)** Location of *Slc40a1* in MMnet**. (B)** Cumulative frequency histogram of relative BMC; n = 8 per genotype. ***p < 0.001 vs. WT by Kolmogorov–Smirnov test. **(C)** Representative X-ray microradiography images of femurs from male $Slc40a1^{flox/flox}$ and $Slc40a1^{\Delta LysMCre}$ mice. Pseudocoloured images indicating low BMC (blue and green) and high BMC (red and pink) are shown in the left panel (scale bar = 1 mm). Micro-CT images of distal femur trabecular bone and mid-diaphysis cortical bone (middle panel) (scale bar = 200 µm). Representative load displacement curves from femur three-point bend testing (right panel). **(D)** Graphs show

trabecular bone volume (BV/TV) and cortical thickness (Ct.Th), femur max load and fracture load; n = 8 mice per genotype. **(F)** Representative TRAP-stained humerus sections from *Slc40a1*$^{flox/flox}$ and *Slc40a1*$^{\Delta LysMCre}$ mice showing osteoclasts stained in red (left panel). Graphs show osteoclast surface (Oc.S/BS) and osteoclast number (N.Oc/BS); n = 5 mice (scale bar = 100µm). **(G)** Representative images of hydroxyapatite resorption (scale bar = 1mm) following *DCSTAMP* and *SLC40A1* si-RNA knockdown. **(H)** Graphs show inhibition of osteoclast hydroxyapatite resorption following *DCSTAMP* and *SLC40A1* si-RNA knockdown (right panel). (Mean±SD from n=4 donors, **P*<0.05, ***P*<0.01, ****P*<0.001 vs scrambled siRNA, one-sample-t test).

Supplementary Figure 1: MMnet is enriched for genes associated with BMD in GWAS **(A)** (Left) Pseudocoloured x-ray microradiography images of femurs from male Lewis (LEW) and Wistar-Kyoto (WKY) rats (low BMC blue and green and high BMC red and pink) showing reduced femur length in WKY animals (scale bar = 1 mm). (Right) Cumulative frequency histogram of relative BMC showing reduced BMC in WKY rats; (n = 4 ***P*< 0.01 vs. WT; Kolmogorov–Smirnov test). **(B)** Representative load displacement curves from femur three-point bend testing. (**C**) Graphs show micro-CT analysis of distal femur trabecular bone (Upper panel), micro-CT analysis from mid-diaphysis cortical bone (middle panel) and femur three-point-bend testing (lower panel) (Mean±SD; n = 4 **P*<0.05, ***P*<0.01 LEW vs WKY student's t-test). (**D**) MMnet comprising 190 *trans*-eQTLs under the master regulatory locus (Trem2, highlighted in red). Each gene in the network is represented as a circle (node), and the genes that are GWAS hits (See also Table 1 and S1) are highlighted in blue. MMnet genes for which knockout mice were available are indicated by thick circles. Connecting lines indicate co-expression between the two transcripts

Supplementary Figure 2: Deletion of *Bcat1* results in increased bone mass and strength due to impaired osteoclast multinucleation and function. (A) Representative X-ray microradiography images of femurs from male WT and *Bcat1*$^{-/-}$ mice. In pseudocoloured images low BMC is indicated by blue and green and high BMC by red and

773 pink (scale bar = 1 mm). **(B)** Cumulative frequency histogram of relative BMC (n = 8). **(C)**
774 Graphs show micro-CT analysis of distal femur trabecular bone, micro-CT analysis of mid-
775 diaphysis cortical bone and femur three-point-bend testing. (Mean±SD; n=8 per genotype as
776 *P<0.05, **P<0.01 vs WT Student's t-test).

777 **Supplementary Figure 3: si-RNA mediated knockdown of MMnet genes in human**
778 **osteoclasts (A)** Inhibition of osteoclast multinucleation following *DCSTAMP* si-RNA
779 knockdown compared with scramble control and cell viability prior to and following
780 transfection. **(B)** Relative mRNA expression of the targeted gene determined by RT-qPCR
781 following si-RNA knockdown (n=4 donors per gene). **(C)** Representative images of TRAP+
782 multinucleated osteoclasts following si-RNA knockdown.

783 **Supplementary Figure 4: An *In silico* filtering strategy prioritises *Slc40a1* (ferroportin)**
784 **for myeloid-targeted gene deletion** (A) Step-wise filtering workflow. (B) 5 candidate genes
785 in MMnet. (C) Percentage of osteoclasts with >4 nuclei after RNAi compared to non-
786 targeting si-RNA; n=4 donors. (D) Representative images of TRAP+ multinucleated
787 osteoclasts (scale bar = 40µm) following *DCSTAMP* and *SLC40A1* si-RNA knockdown. Data
788 analysed using a one-sample-t test and presented as mean±SD with significances defined
789 as *P<0.05, **P<0.01, ***P<0.001.

790 **Supplementary Figure 5: Myeloid-specific deletion of *Ferroportin* results in increased**
791 **bone mass and strength due to impaired osteoclast multinucleation and function. (A)**
792 Graphs show micro-CT analysis of distal femur trabecular bone, micro-CT analysis of mid-
793 diaphysis cortical bone and femur three-point-bend testing in male mice. (Mean±SD; n=8 per
794 genotype as *P<0.05, **P<0.01 $Slc40a1^{\Delta LysMCre}$ *vs* $Slc40a1^{flox/flox}$ Student's t-test). **(B)**
795 Representative micro-CT images of distal femur trabecular bone and mid-diaphysis cortical
796 bone in $Slc40a1^{\Delta LysMCre}$ *and* $Slc40a1^{flox/flox}$ female mice (scale bar = 200 µm). **(C)**
797 Representative load displacement curves from three-point bend testing of femurs from
798 $Slc40a1^{\Delta LysMCre}$ *and* $Slc40a1^{flox/flox}$ female mice. **(D)** Graphs show micro-CT analysis of distal
799 femur trabecular bone, micro-CT analysis of mid-diaphysis cortical bone and femur three-

800 point-bend testing in female mice: Mean±SD; n=8 per genotype, *P<0.05, **P<0.01

801 *Slc40a1*$^{\Delta LysMCre}$ *vs Slc40a1*$^{flox/flox}$, Student's t-test.

802

Figure 1

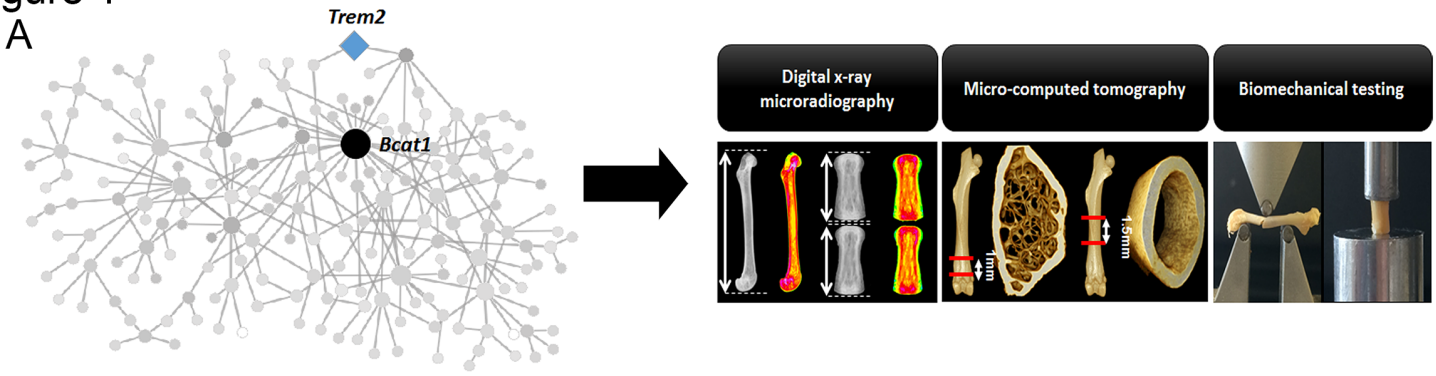
A
Trem2
Bcat1
Digital x-ray microradiography
Micro-computed tomography
Biomechanical testing
1mm
1.5mm

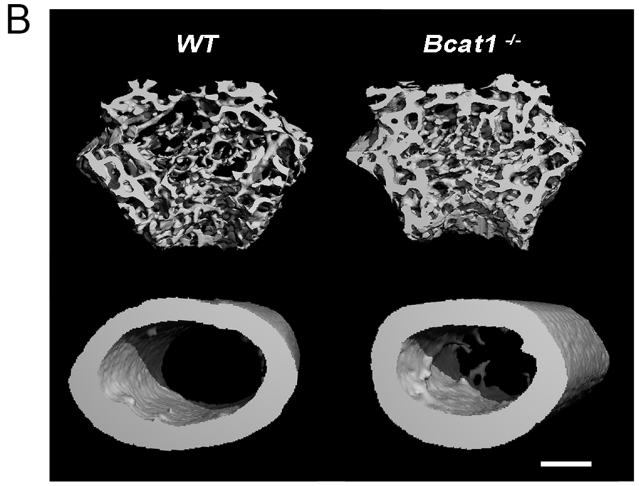
B
WT
Bcat1 -/-

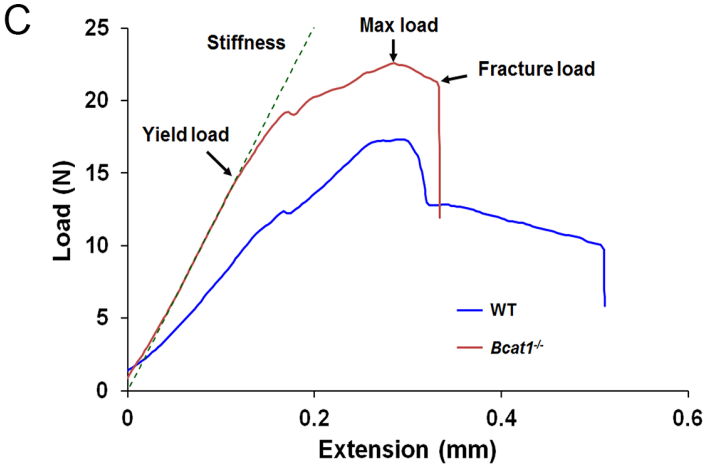
C
Stiffness
Max load
Fracture load
Yield load
Load (N)
Extension (mm)
WT
Bcat1-/-

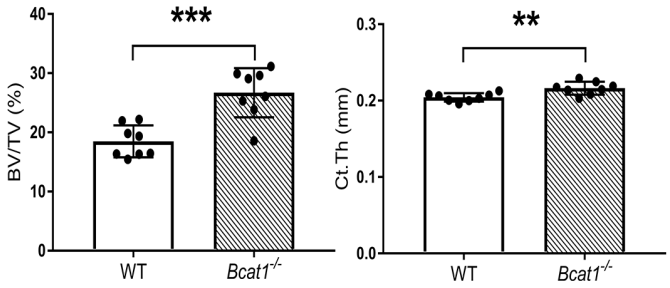
BV/TV (%)
Ct.Th (mm)
***
**
WT
Bcat1-/-

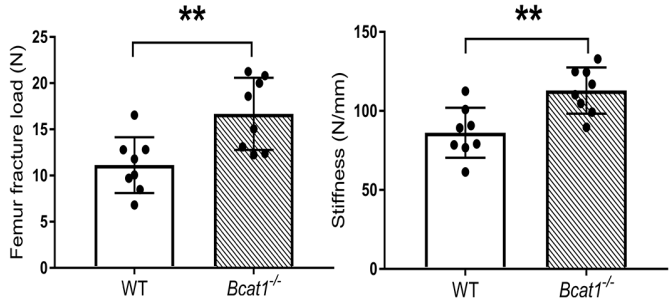
Femur fracture load (N)
Stiffness (N/mm)
**
**
WT
Bcat1-/-

D

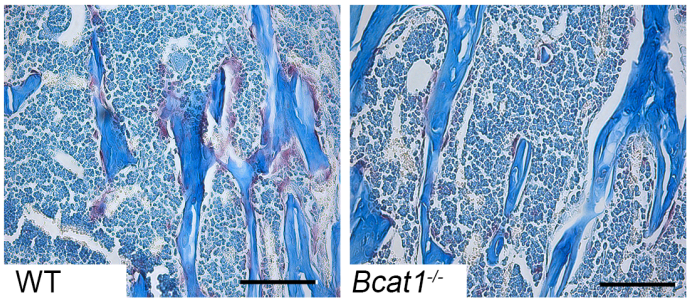
WT
Bcat1-/-

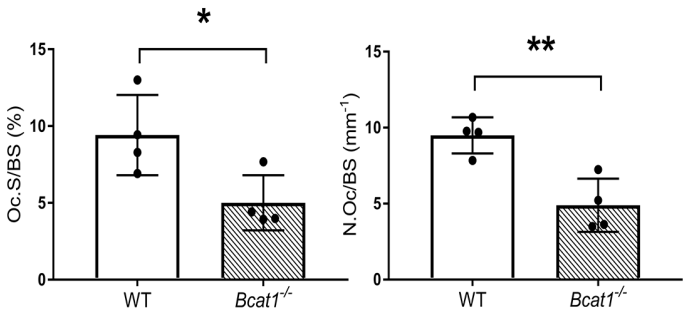
Oc.S/BS (%)
N.Oc/BS (mm-1)
*
**
WT
Bcat1-/-

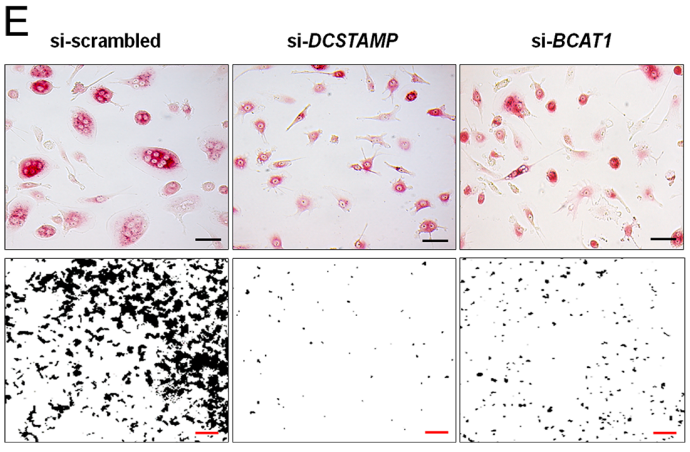
E
si-scrambled
si-DCSTAMP
si-BCAT1

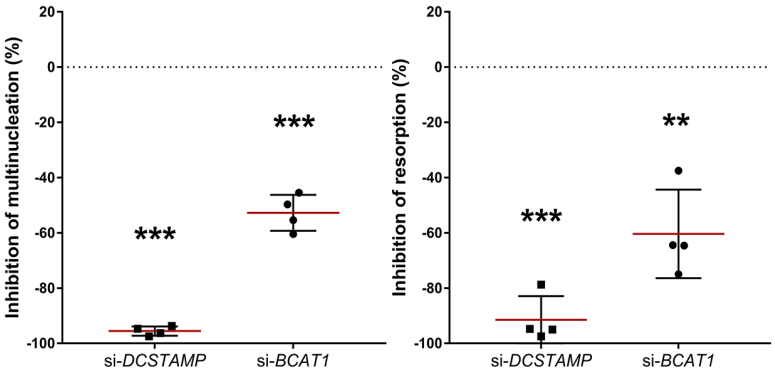
F
Inhibition of multinucleation (%)
Inhibition of resorption (%)
***
***
***
**
si-DCSTAMP
si-BCAT1

Figure 2

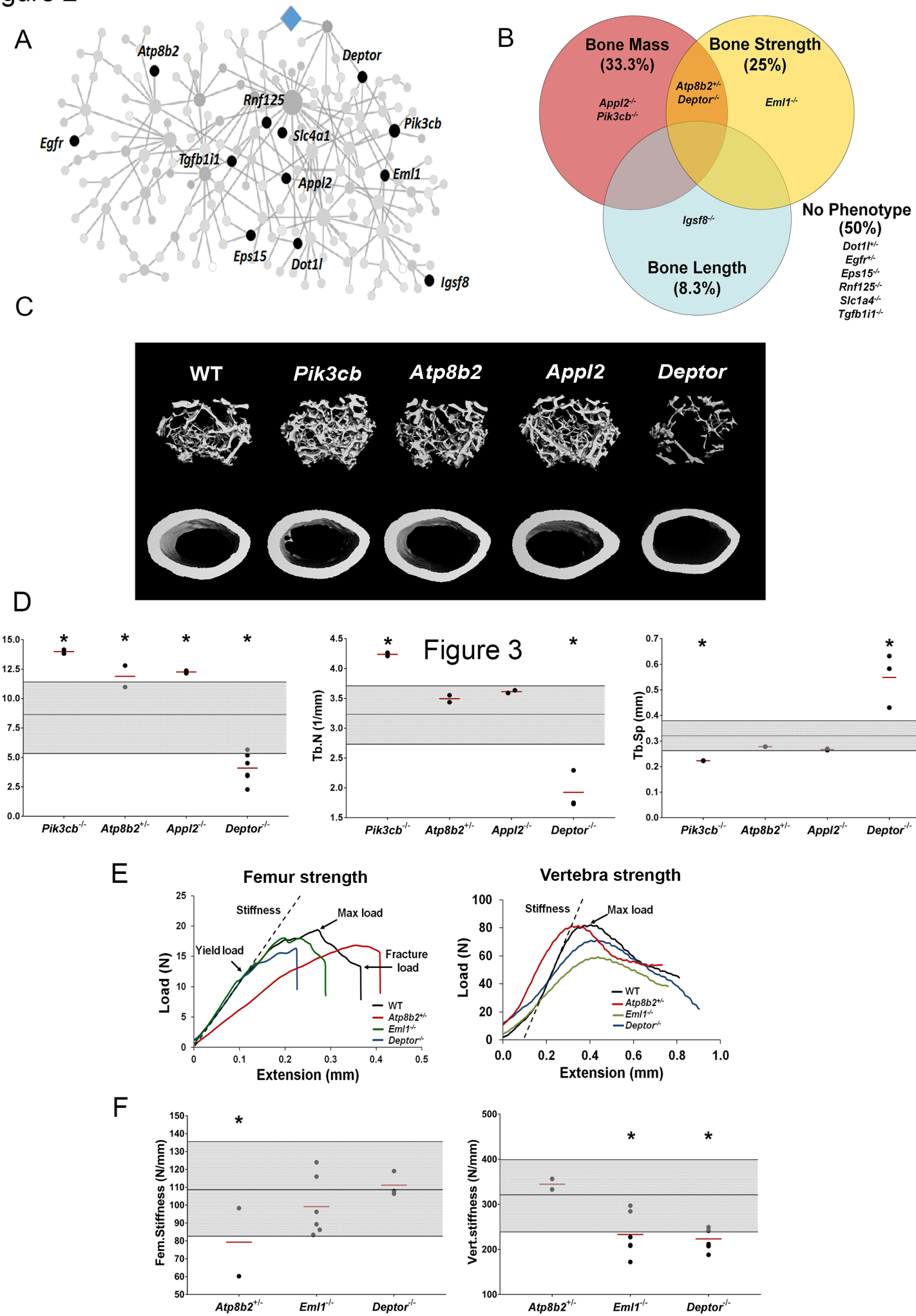

Figure 3

Figure 3

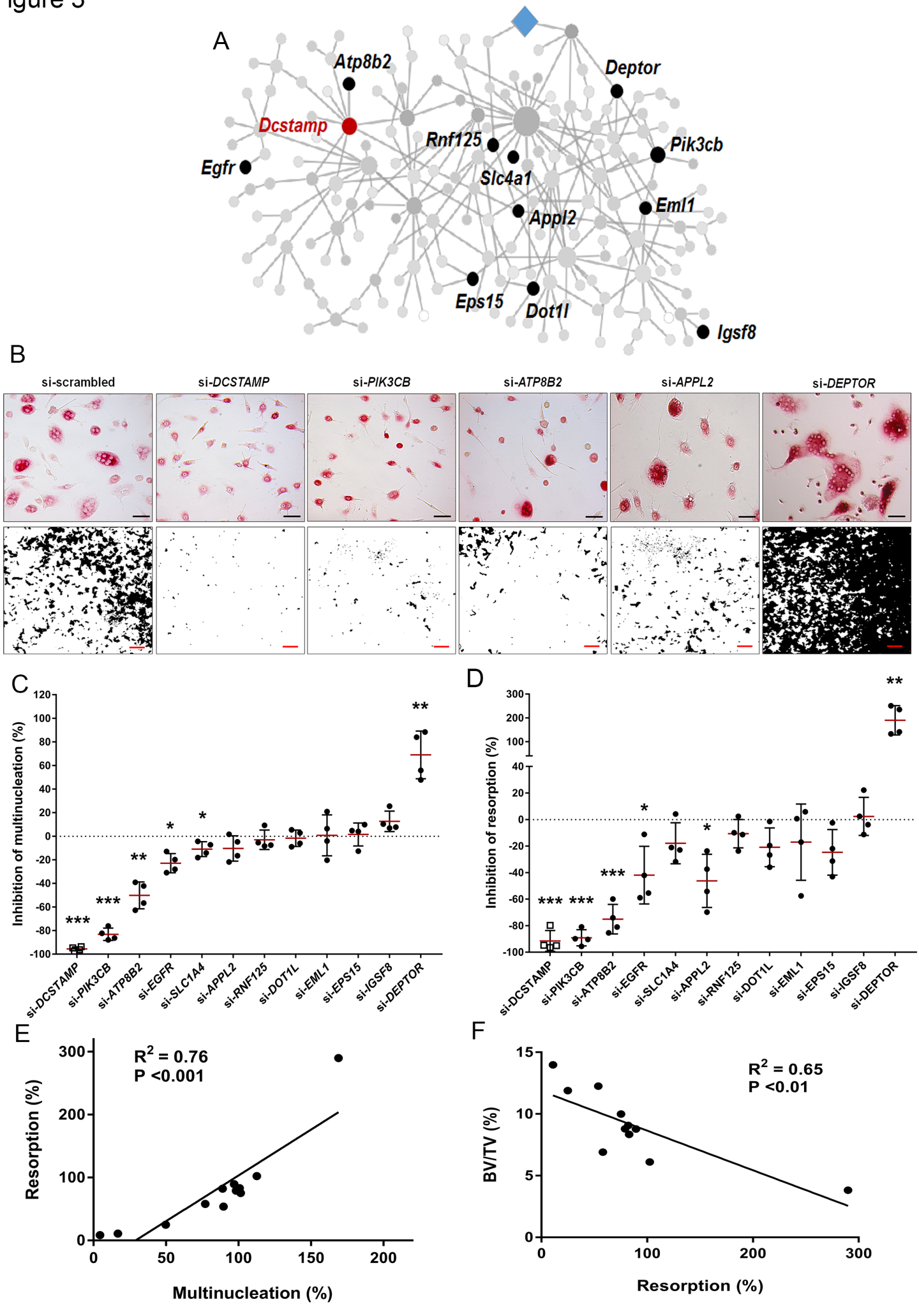
A
Atp8b2
Deptor
Dcstamp
Rnf125
Pik3cb
Egfr
Slc4a1
Eml1
Appl2
Eps15
Dot1l
Igsf8
B
si-scrambled
si-DCSTAMP
si-PIK3CB
si-ATP8B2
si-APPL2
si-DEPTOR
C
Inhibition of multinucleation (%)
si-DCSTAMP
si-PIK3CB
si-ATP8B2
si-EGFR
si-SLC1A4
si-APPL2
si-RNF125
si-DOT1L
si-EML1
si-EPS15
si-IGSF8
si-DEPTOR
D
Inhibition of resorption (%)
si-DCSTAMP
si-PIK3CB
si-ATP8B2
si-EGFR
si-SLC1A4
si-APPL2
si-RNF125
si-DOT1L
si-EML1
si-EPS15
si-IGSF8
si-DEPTOR
E
R2 = 0.76
P <0.001
Resorption (%)
Multinucleation (%)
F
R2 = 0.65
P <0.01
BV/TV (%)
Resorption (%)

Figure 4

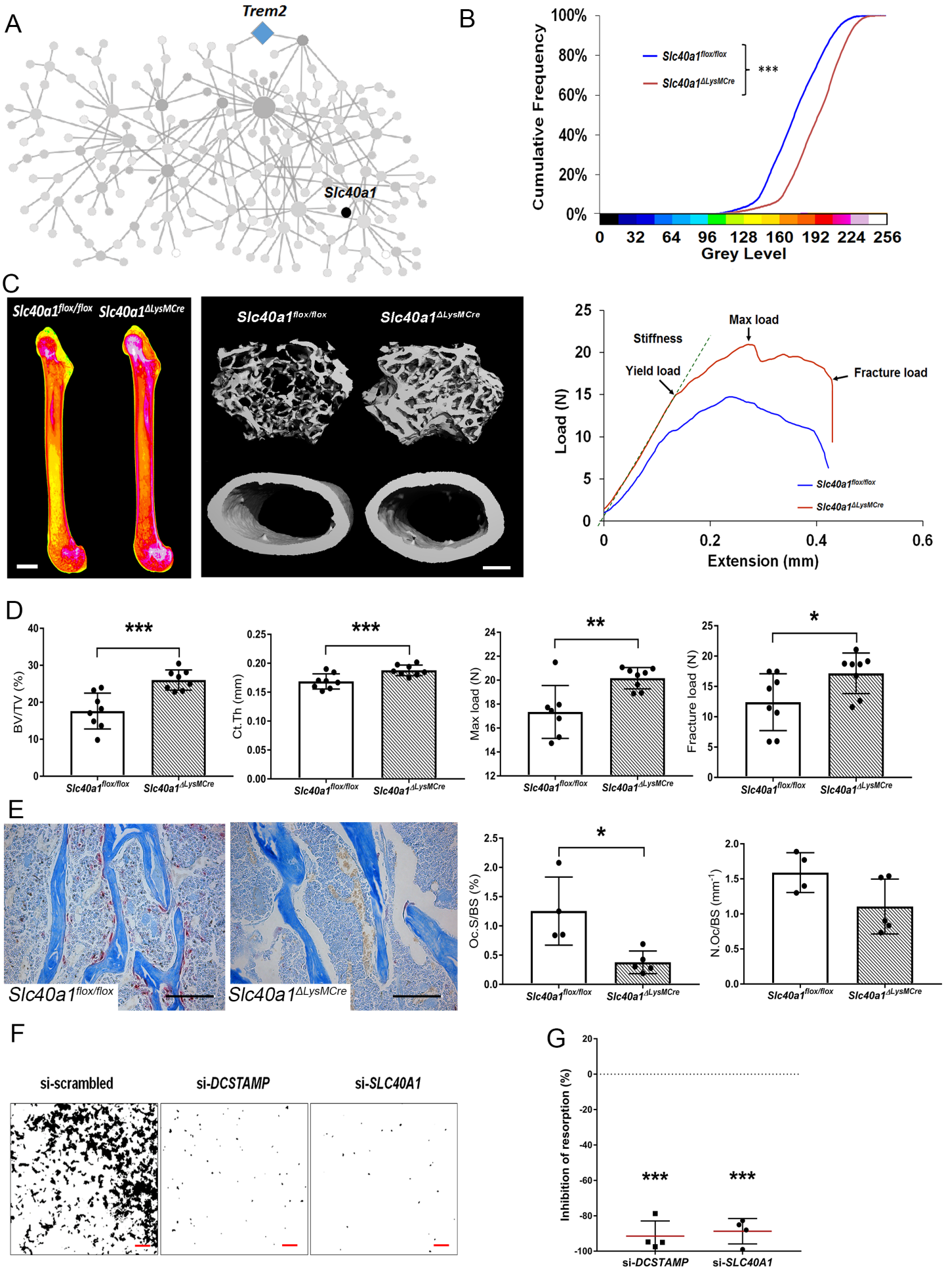
A
Trem2
Slc40a1
B
Cumulative Frequency
100%
80%
60%
40%
20%
0%
Slc40a1flox/flox
Slc40a1ΔLysMCre
***
0 32 64 96 128 160 192 224 256
Grey Level
C
Slc40a1flox/flox Slc40a1ΔLysMCre
Slc40a1flox/flox Slc40a1ΔLysMCre
Load (N)
Stiffness
Max load
Yield load
Fracture load
Slc40a1flox/flox
Slc40a1ΔLysMCre
0 0.2 0.4 0.6
Extension (mm)
D
BV/TV (%)
Ct.Th (mm)
Max load (N)
Fracture load (N)
***
***
**
*
Slc40a1flox/flox
Slc40a1ΔLysMCre
E
Slc40a1flox/flox
Slc40a1ΔLysMCre
Oc.S/BS (%)
N.Oc/BS (mm-1)
*
Slc40a1flox/flox
Slc40a1ΔLysMCre
F
si-scrambled
si-DCSTAMP
si-SLC40A1
G
Inhibition of resorption (%)
***
***
si-DCSTAMP
si-SLC40A1

Supplementary Figure 1

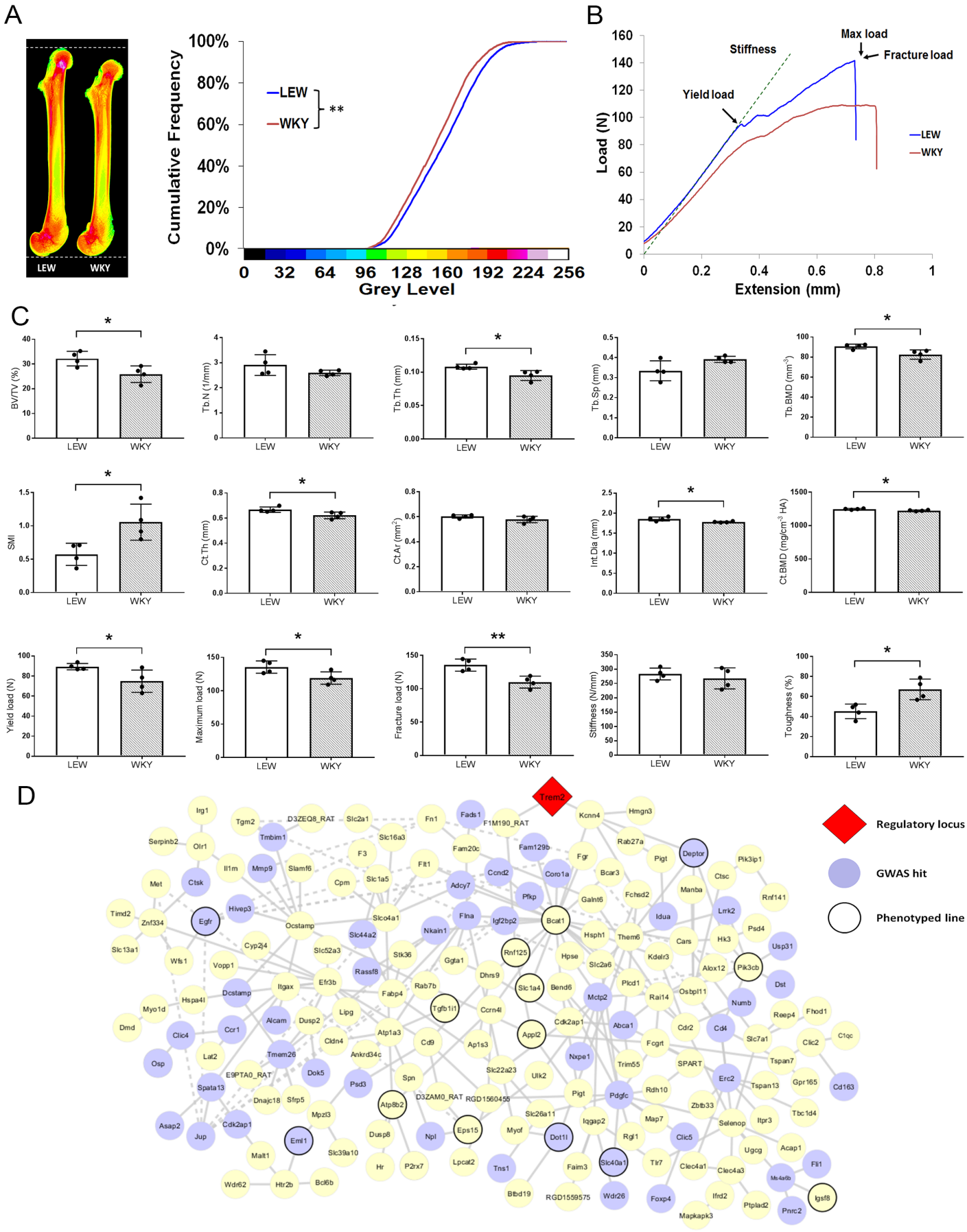

Supplementary figure 2

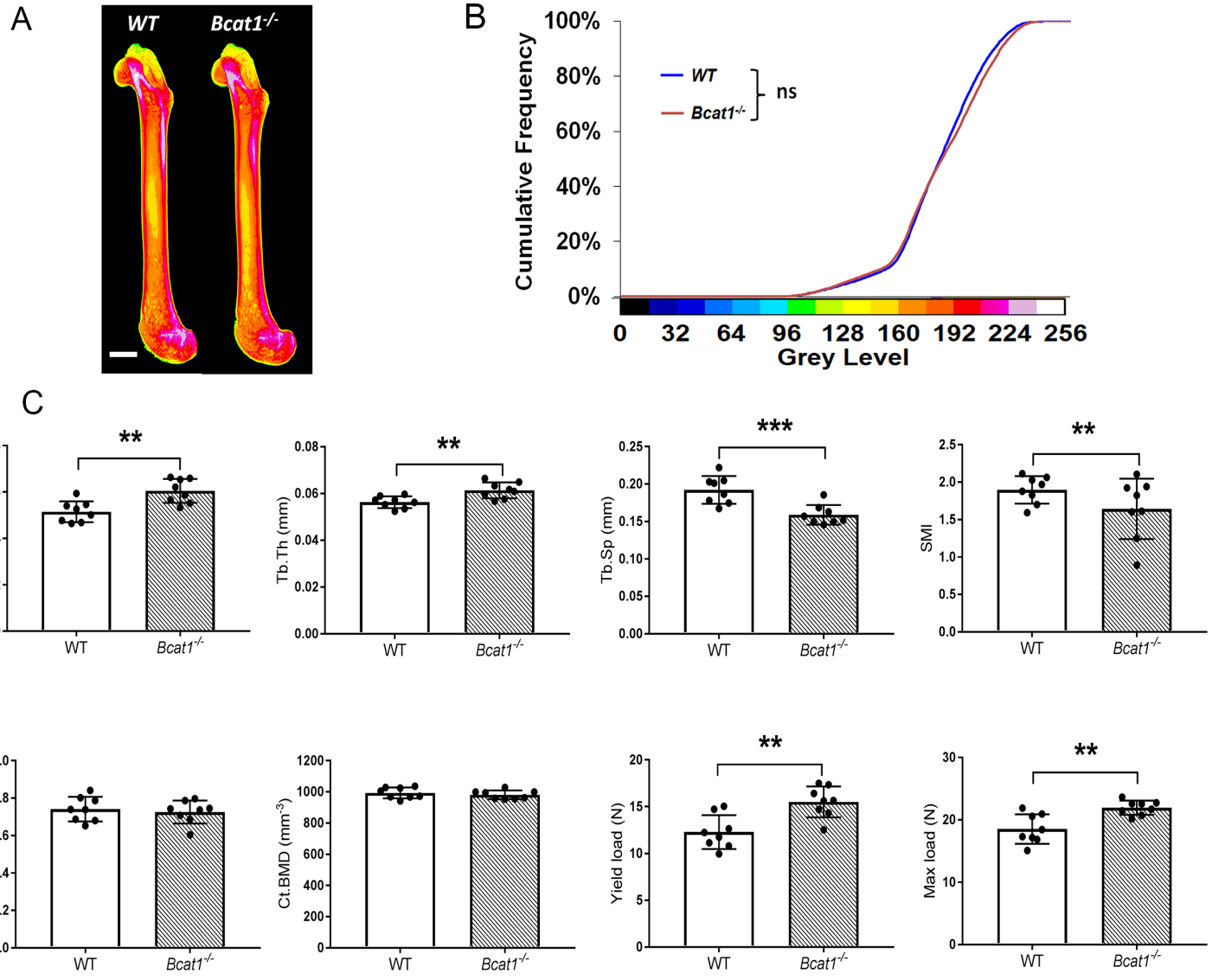

Supplementary Figure 3

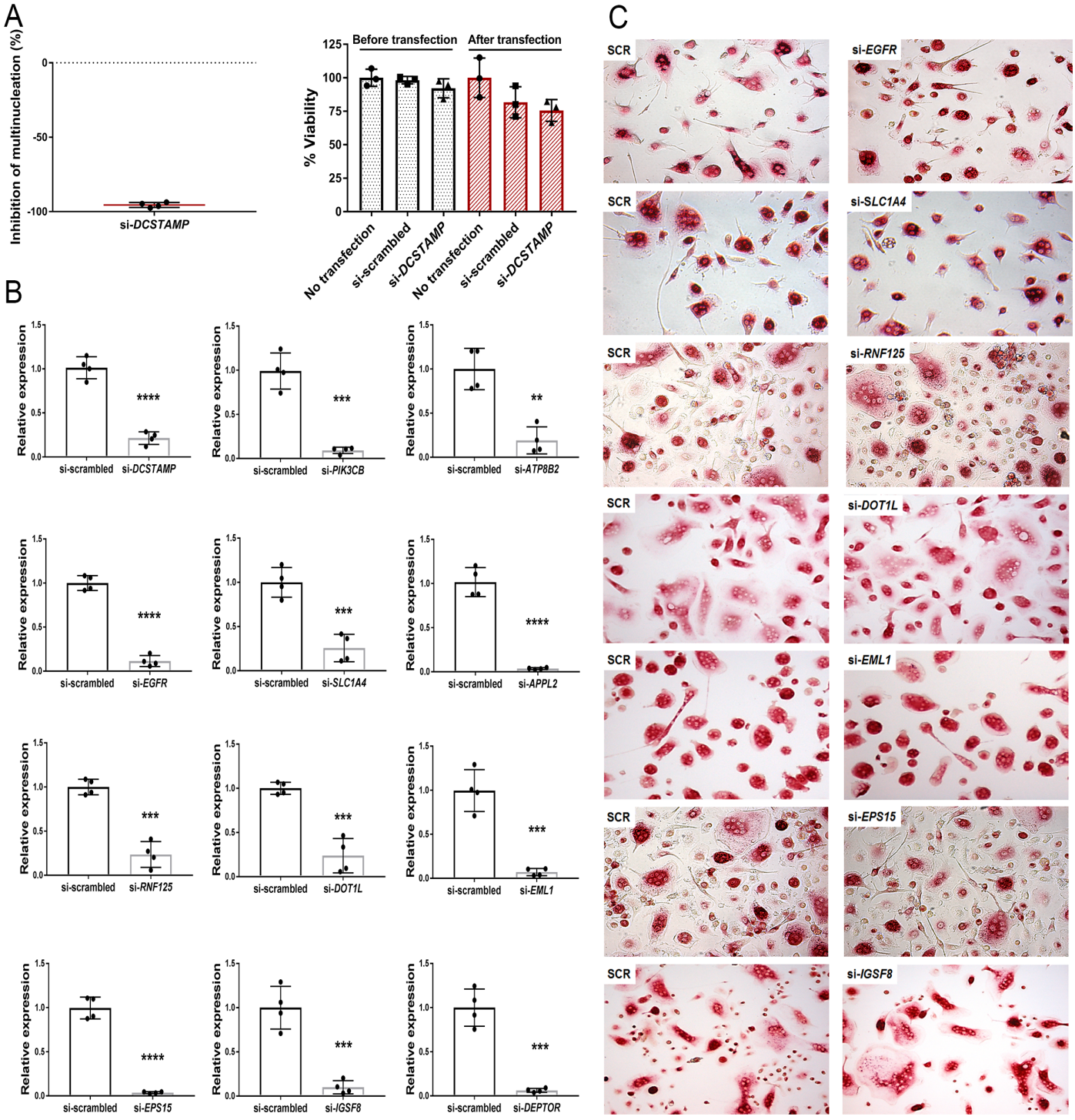

Supplementary Figure 4

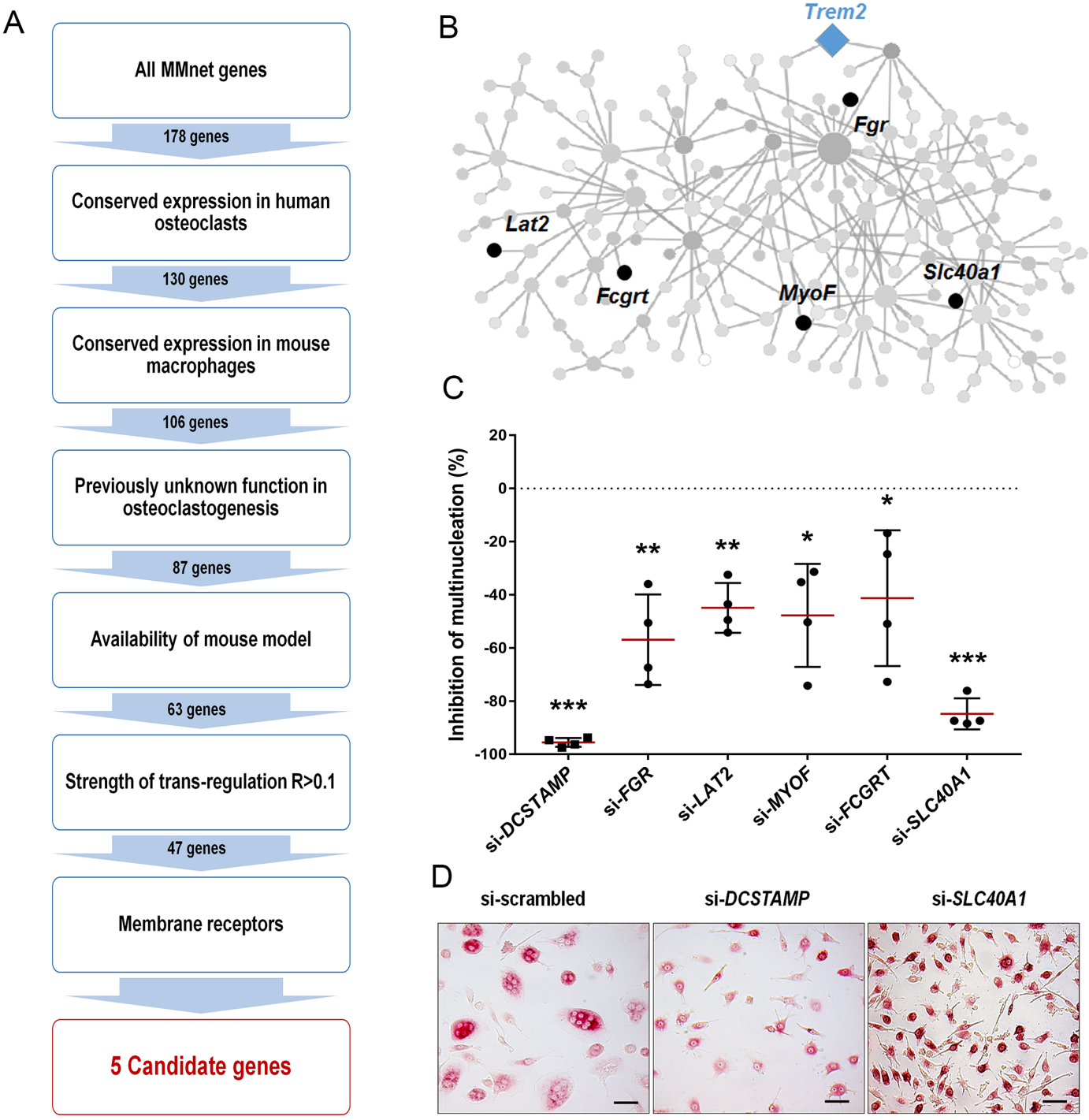

Supplementary Figure 5